

The multiplicity of the subgiant branch of ω Centauri: Evidence for prolonged star formation¹

S. Villanova¹, G. Piotto¹, I. R. King², J. Anderson³, L. R. Bedin⁴, R. G. Gratton⁶, S. Cassisi⁵, Y. Momany^{1,6}, A. Bellini¹, A. M. Cool⁷, A. Recio-Blanco⁸, and A. Renzini⁶

ABSTRACT

We present metallicity measurements based on GIRAFFE@VLT spectra of 80 subgiant-branch stars of the Galactic globular cluster ω Centauri. The VLT spectroscopic data are complemented by color-magnitude diagrams from high-accuracy photometry on a $\sim 10 \times 10$ arcmin² mosaic of ACS/*HST* images centered on the cluster center, and on multicolor images of a $\sim 34 \times 33$ arcmin² field, taken with the WFI@ESO2.2m camera. Our main purpose was to combine photometric data with spectroscopic data, in the hope of teasing apart some of the population mysteries that neither data set can answer on its own. We have obtained the [Fe/H] abundance for each of the 80 target stars, and the abundances of C, N, Ca, Ti, and Ba for a subset of them, by comparison with synthetic spectra. We show that stars with [Fe/H] < -1.25 have a large magnitude spread on the flat part of the SGB. We interpret this as empirical evidence for an age spread. A relative age has been obtained for each star, from theoretical isochrones for its metallicity, α -enhancement, and presumed He content. We have identified four distinct stellar groups within the SGB region: (i) an old, metal-poor group ([Fe/H] ~ -1.7); (ii) an old, metal-rich group ([Fe/H] ~ -1.1); (iii) a young (up to 4–5 Gyr younger than the old component) metal-poor group ([Fe/H] ~ -1.7); (iv) a young, intermediate-metallicity ([Fe/H] ~ -1.4) group, on average 1–2 Gyr younger than the old metal-poor population, and with an age spread that we cannot properly quantify with the present sample. In addition, a group of SGB stars are spread between the intermediate-metallicity and metal-rich branches of the SGB. We tentatively propose connections between the SGB stars and both the multiple main sequence and the red giant branch. Finally, we discuss the implications of the multiple stellar populations on the formation and evolution of ω Cen. The spread in age within each population establishes that the original system must have had a composite nature.

Subject headings: Galaxy: abundances – globular clusters: NGC 5139 – Hertzsprung-Russell diagram

¹Dipartimento di Astronomia, Università di Padova, Vicolo dell'Osservatorio 3, I-35122 Padua, Italy

²Department of Astronomy, University of Washington, Box 351580, Seattle, WA 98195-1580

³Department of Physics and Astronomy, Mail Stop 108, Rice University, 6100 Main Street, Houston, TX 77005

⁴European Southern Observatory, Karl-Schwarzschild-Strasse 2, D-85748 Garching, Germany

⁵INAF-Osservatorio Astronomico di Collurania, via Mentore Maggini, 64100 Teramo, Italy

⁶INAF-Osservatorio Astronomico di Padova, Vicolo

dell'Osservatorio 5, I-35122 Padua, Italy

⁷Department of Physics and Astronomy, San Francisco State University, 1600 Holloway Avenue, San Francisco, CA 94132

⁸Observatoire de la Côte d'Azur, Dpt. Cassiope UMR 6202 B.P. 4229, 06304 Nice Cedex 4, France

¹Based on FLAMES+GIRAFFE@VLT observations under the DDT program 272.D-5065(A), and on observations with the NASA/ESA *Hubble Space Telescope*, obtained at the Space Telescope Science Institute, which is operated by AURA, Inc., under NASA contract NAS 5-26555

1. Introduction

Omega Centauri is a peculiar and enigmatic object: it appears to be a globular cluster (GC), but it has a complex stellar population, and with its unusual mass ($M \sim 3 \times 10^6 M_\odot$) it has often been suggested to be the remains of a larger stellar system. It has received a large amount of attention; for a review see Meylan 2003. The most provocative recent result (Anderson 1997, Bedin et al. 2004, hereafter B04) was the discovery that over a range of at least two magnitudes the main sequence splits into a red branch and a blue one. Follow-up spectroscopic studies at medium resolution led to even more enigmatic results (Piotto et al. 2005, hereafter P05): contrary to any expectation from canonical stellar models, the bluer branch of the MS is more metal-rich than the red one. At the moment, the only explanation of the photometric and spectroscopic properties of the double main sequence that is at all plausible is that the bluer branch of the MS has an unusually high helium content (B04, Norris 2004, P05, Lee et al. 2005).

It has been suggested that this unusual He-rich population might come from material contaminated by the ejecta of massive ($25 M_\odot$, Norris 2004), or slightly less massive (10–14 M_\odot , P05) supernovae, or from rapidly rotating low-metallicity massive stars (Maeder & Meynet 2006), or from intermediate-mass asymptotic-giant-branch stars (Izzard et al. 2004). None of these hypotheses has been directly supported by observation. A detailed study of the chemical abundances of the different populations identified in ω Cen is badly needed in order better to understand the complex star-formation history of this cluster.

In the present paper we continue the photometric and spectroscopic investigation started in B04 and P05, giving further results on the double main sequence but concentrating our main attention on the region of the subgiant branch (SGB), which is even more complex than the MS, because of the presence of many different SGBs (Ferraro et al. 2004, B04). It is the combination of spectroscopy of SGB stars with high-accuracy photometry that will allow us to shed new light on the star-formation history of ω Cen.

In Section 2 we present the photometric data. The new color-magnitude diagrams (CMDs) are

shown and discussed in Section 3, while the spectroscopic data are presented in Section 4. Section 5 deals with the terminology of populations. In Section 6 we discuss the abundance measurements, which in Section 7 are compared with the results of P05 and of other investigators. Section 8 discusses the implications of the photometric and the spectroscopic results on the SGB multiplicity. In Section 9 we present relative age measurements for the spectroscopic target stars. A final section discusses the implications of the observational facts presented in this paper for the stellar population in ω Centauri and for the origin of this anomalous cluster.

2. Photometry

2.1. HST data

Our photometric *HST* study is based on a mosaic of 3×3 *HST* ACS/WFC fields taken in GO-9442 (PI Cool). Each of the fields has exposures of $3 \times 340 + 12$ sec. in F435W, $3 \times 340 + 8$ sec. in F625W, and 4×440 sec. in F658N (H_α). The images were reduced using `img2xym_WFC.09x10`, which is a publicly available FORTRAN program described in Anderson & King (2006). The program finds and measures each star in each exposure, by fitting a spatially variable empirical PSF. We collated the independent measurements of the stars into a master star list that covers the entire mosaic field. For each star we constructed an average magnitude in each band, and computed errors from the agreement among the independent exposures. The instrumental magnitudes were transformed into the ACS Vega-mag flight system following the procedure given in Bedin et al. (2005), using the zero points of Sirianni et al. (2005). To calculate our aperture corrections we used single DRZ images with the longer exposure time.

Figure 1 shows our color-magnitude diagram (CMD). We believe that this is the most accurate CMD ever published for this cluster. In the present paper we discuss the subgiant region and the upper part of the main sequence; later papers will deal with other features.

2.2. WFI data

The ground-based component of our photometry is based on 187 images taken from 1999 to 2003 with the WFI@ESO2.2m camera (hereafter

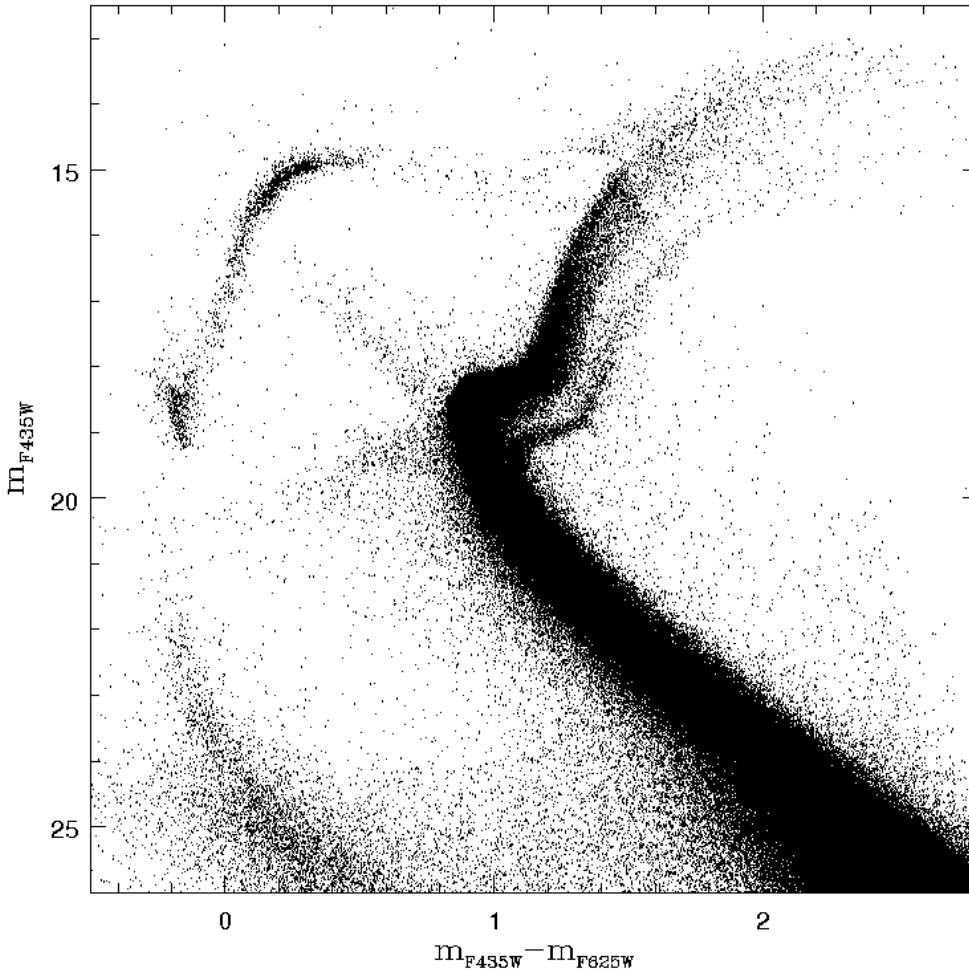


Fig. 1.— Our CMD of ω Centauri, from the photometry of more than a million stars in the central 3×3 ACS fields.

WFI). Exposure times cover the range 5–1800 seconds in Johnson U , B , and V , and in Cousins R_C and I_C , plus some observations with the 665 nm and 658 nm narrow-band filters. The images were reduced using `img2xym_WFI`, software developed specifically for the WFI camera and described in Anderson et al. (2006). The program works in a way quite similar to `img2xym_WFC.09x10`, from which it was derived. We carried out photometry and astrometry of about 30,000 stars. Taking advantage of the 4-year temporal baseline, we derived proper motions, which, after application of corrections for differential chromatic refraction,

allowed a very good cluster/field star separation.

The whole WFI data set will be the subject of a separate paper. For the present study we used the WFI data to choose the spectroscopic targets and to derive their atmospheric parameters.

3. Structure within regions of the CMD

Our new CMDs provide us with three kinds of information. First, they allow us to delineate sequences better than we could before. Second, in several cases they show us connections between populations in different regions of the CMD.

Third, when combined with spectroscopic abundances for a modest number of stars, they will provide a crucial correspondence between abundance-based populations and photometry-based ones.

3.1. Main sequence

With our new more accurate photometry we can now study the double part of the main sequence more carefully. Since the split is not at all clear in the MS area of Fig. 1, we plot in the left panel of Figure 2 only a randomly chosen 4% of the stars, while the middle panel shows a randomly chosen 6% of the stars on an expanded color scale, with a hand-drawn fiducial sequence subtracted out. These percentages were chosen to reduce the number of stars to a level that would enable these two plots to give a clear visual impression of the MS split. Our quantitative result is in the right-hand panel, which shows histograms of the colors of all of the stars, in quarter-magnitude intervals. The distributions corresponding to the two sequences overlap, but they clearly define two groups of stars, the first at $m_{F435W} - m_{F625W} \sim 0$ in the straightened figure and the second at $m_{F435W} - m_{F625W} \sim -0.05$ —the rMS and bMS of B04, respectively—groups that are quite distinct, at least in the magnitude interval $20.5 < m_{F435W} < 22.5$. The two MSs tend to merge at brighter and fainter magnitudes. No additional splits are apparent within these two sequences (See also the discussion in Sollima et al. 2006b.)

We can also analyze another population aspect of the MS. As was noted by Sollima et al. (2005a, hereafter S05), in Fig. 1 the detached red-giant sequence RGB-a apparently continues through the subgiant region (SGB-a) and then merges into the main sequence. With our new photometry we can follow it part way down the MS, as shown in Figure 3. In the histograms the sequence, whose main-sequence turnoff in Fig. 1 is at $B = 19.4$, is visible as a secondary maximum down to $B = 20$, and appears to create an extension of the color distribution down at least to $B = 21$. By analogy with RGB-a, we call this MS-a.

In Fig. 2 and Fig. 3 we can see that where the bMS and rMS are better separated, MS-a is blended with the rMS. Because of this blend, we can measure the fraction of stars belonging to the bMS only with respect to the total MS population. We find that the bMS contains $\sim 33\%$ of the

main-sequence stars. This value will be useful in our later discussion. Here we note that Sollima et al. (2006b) have found a strong radial gradient for the ratio of bMS/rMS stars, for distances $r > 8$ arcmin from the cluster center. Interestingly enough, while we confirm their external gradient with independent *HST* data, the radial distribution of the bMS/rMS stars within our 3×3 ACS field is flat (Bellini et al., in preparation). Therefore the fraction of bMS stars with respect to the other main sequence stars stays constant within the *HST* field analyzed in the present paper.

3.2. Subgiant region

We now turn to the subgiant region, which in the rest of this paper we will use as a key to the multiple populations of ω Centauri. Figure 4 shows an enlargement of that part of the CMD. This region is even more complex than the main sequence. In the lower part of the figure is a histogram of the star numbers within the parallelogram shown, summed parallel to the short edge and plotted against a coordinate (X) that runs along the long edge, with zero point at the heavy line in the upper panel. Along with the four distinct peaks labeled A, B, C, and D, there is a broad distribution of stars in the interval $-0.8 < X < -0.45$. These populations are better identified in the Hess diagram of the region that is plotted in Fig. 5. We will refer to them as SGB Groups A, B, C, and D.

Here we are facing important evidence that we will try to interpret in later sections: the number distribution of the SGB stars across the CMD is significantly different from what we would have expected from the distribution of the stars across the branches of the main sequence. The rMS and bMS of B04 correspond to two distinct groups, separated in color and with different metal and helium content (P05), and without any apparent substructures (as shown in Fig. 2). To these two sequences we need to add MS-a, on the red side of the rMS, which we have clearly identified in Fig. 3, and which apparently continues into SGB Group D and then into RGB-a. From the distribution of the stars on the MS, we would have expected to see only three distinct SGBs, one including all of the stars that have a metallicity similar to that of the bMS, one with the stars that have the metallicity

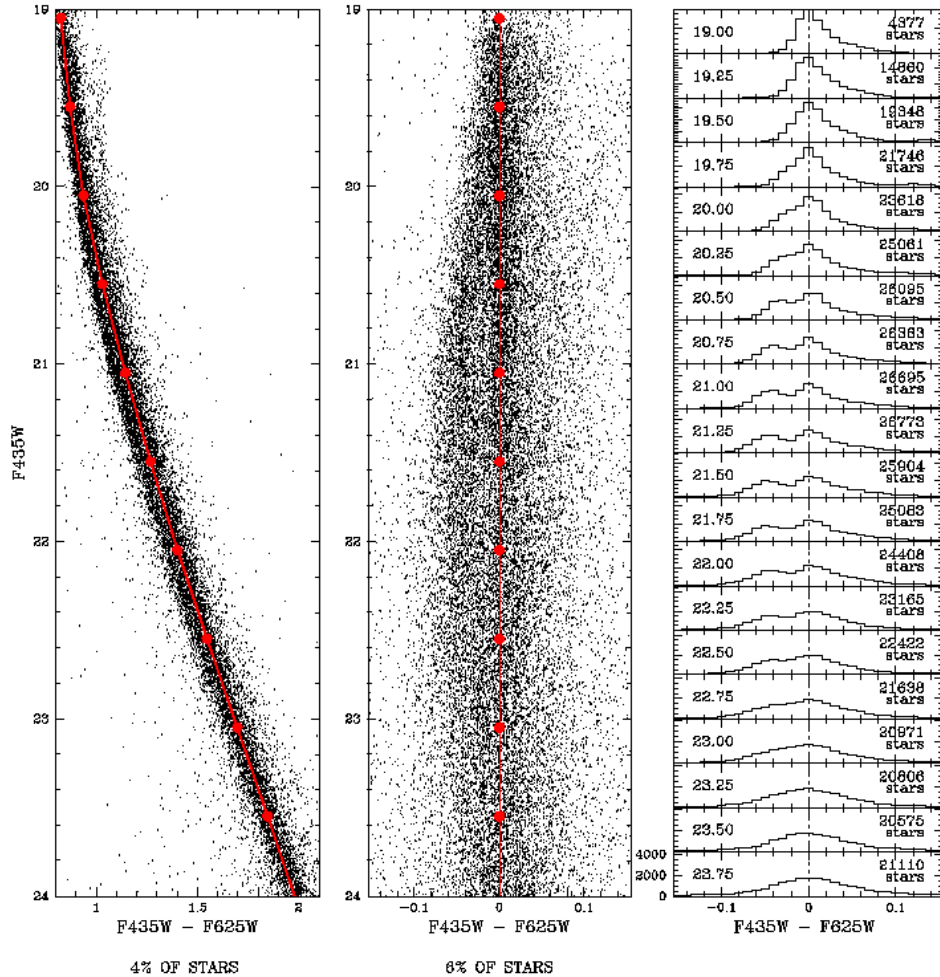


Fig. 2.— Enlargement of the CMD of Fig. 1, showing the double main sequence of B04. In the central panel we have subtracted from the color of the red MS the color of a fiducial line, drawn by hand. The right-hand panel shows the color distribution of the points plotted in the central panel.

of the RMS, and a third component coming from the reddest MS of Fig. 3, which is identified with SGB Group D. Contrary to these expectations, the SGB region shown in Fig. 5 is split into many different branches, with stars distributed into a CMD region spanning 0.6–0.8 magnitude in m_{F435W} , if we exclude SGB Group D, or more than 1.2 magnitudes if we include it. It is important to note that this magnitude range is more than twice as large as the 0.4–0.5 magnitude that would be expected from the metallicity range covered by the ω Cen stars if we assume that all of them have the same

age, as can be seen from isochrones published by Pietrinferni et al. (2004, 2006).

3.3. Continuity between regions

The continuity of the sequences that correspond to the four SGB groups is fairly clear within the SGB region, but it is not always obvious how they connect with sequences in other parts of the CMD (both MS and RGB). In particular, it is not at all clear how SGB Groups B and C connect with the MS. At this stage, however, we can make the

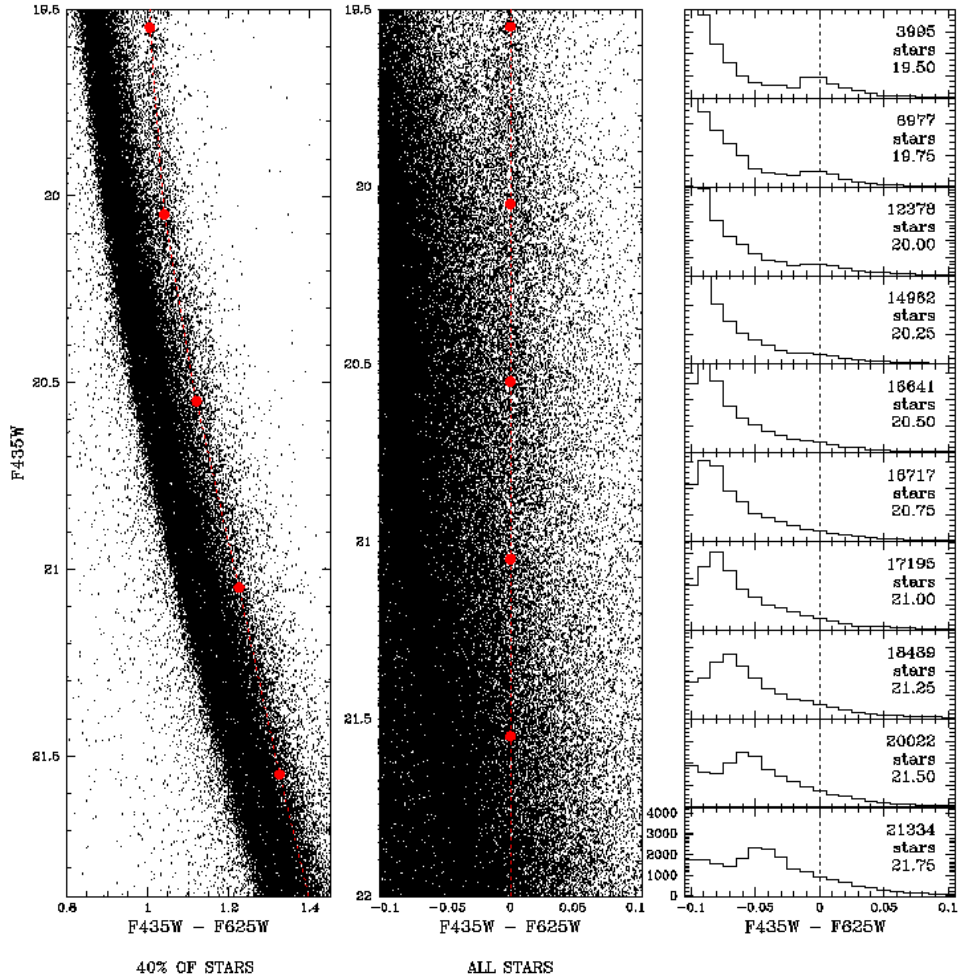


Fig. 3.— The reddest branch of the main sequence, which connects with SGB-a. In the left panel is an enlargement of part of the CMD, with a fiducial sequence drawn through the reddest branch. In the middle panel the colors of the fiducial sequence are subtracted off, and at the right are histograms of 0.25-magnitude intervals.

following simple connections:

- SGB Group D connects with the reddest branch of the MS, MS-a, as can be seen from Figs. 3–6. Figure 6 is very similar to panel *e* of Fig. 1 in B04, but to avoid confusion it displays a randomly selected subsample of the stars in the ACS fields. As in B04, here we use the $m_{H\alpha}$ vs. $m_{F435W} - m_{H\alpha}$ CMD in order better to show the separation between the two branches in the upper part of the

MS.

- It is clear that the rMS continues into the upper SGB (which in the preceding subsection we named Group A), as shown in Figure 6.
- The bMS can be followed up nearly to the turn-off, as can be seen in Fig. 6. It then continues into the SGB region, where it is no longer possible to follow it clearly.

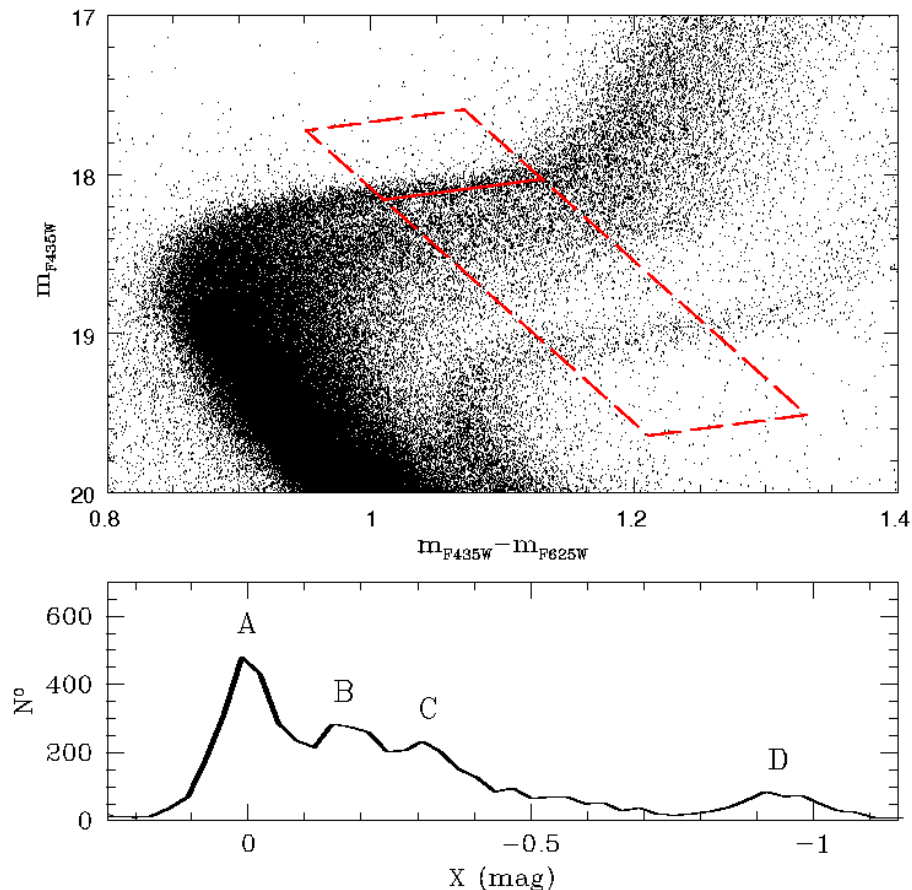


Fig. 4.— Top: enlargement of Fig. 1 to show the SGB region better. Bottom: distribution of the stars in the parallelogram. (See text for details.)

It is also clear that SGB Group A cannot account for all of the rMS stars. We estimated the rough number of stars in each group of Figs. 4 and 5 by fitting four Gaussians centered on the four peaks of the histogram of the lower panel of Fig. 4 (see Section 8). SGB Group A contains about 33% of the SGB stars, much less than the fraction of MS stars that belong to the rMS (in our *HST* field, about two thirds). We will resume this discussion at the end of Section 8, where we will be able to combine this information with what comes from the spectroscopic analysis.

4. Spectroscopic observations and data reduction

The spectroscopic data come from ESO DDT time [proposal 272.D-5065(A)], and were collected in April–May 2004 with FLAMES@VLT+GIRAFFE. The sky was clear, and the typical seeing was 0.8 arcsec. We used the MEDUSA mode, which obtains 132 spectra simultaneously. To have enough S/N , and in order to cover the wavelengths of interest, in the spectrograph we used the LR2 set-up, which gives $R = 6400$ in the 3960–4560 Å range. Thirty-four GIRAFFE fibers were placed on stars of the blue and red branches of the MS; the results from those spectra have

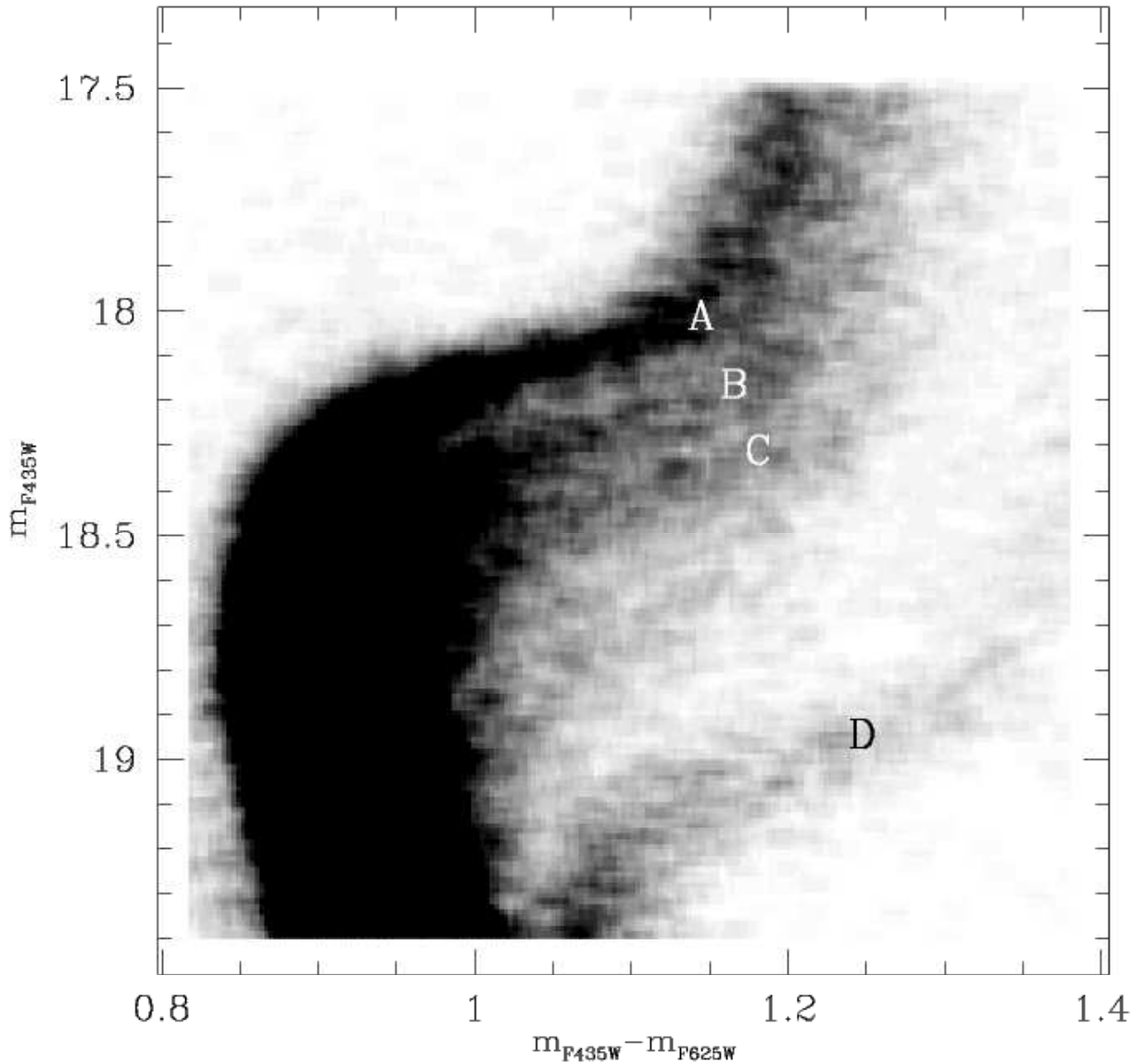


Fig. 5.— Hess diagram of the SGB region, to show its complex structure. At least four agglomerates of stars can be distinguished (marked A, B, C, D), with additional stars distributed between the faintest group (SGB-a = D) and the three brighter groups.

already been presented in P05. The remaining fibers were placed on SGB stars (88 fibers) and on the sky (10 fibers). Twelve one-hour spectra were obtained for each target.

Twenty-two target stars were selected from the

3×3 mosaic of *HST* fields presented in Section 2.1. An additional 66 SGB stars were selected from the ground-based $\sim 34' \times 33'$ ESO/WFI@2.2m field. Its coverage includes the region of the *HST* fields for which photometric results were presented in

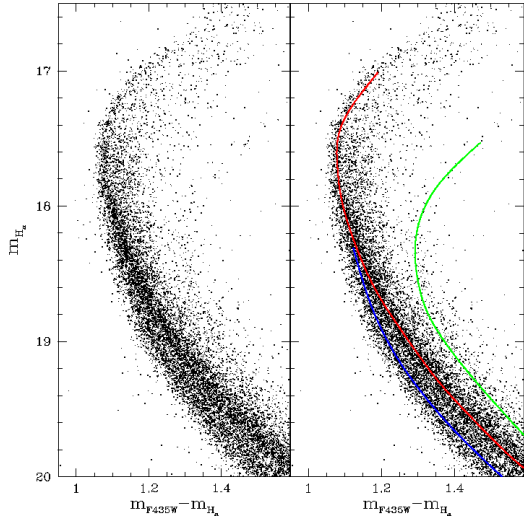


Fig. 6.— (left) $m_{H\alpha}$ vs. $m_{F435W} - m_{H\alpha}$ CMD for the ACS fields. (right) Fiducial lines drawn by hand help to show the connections between the MS and the SGB. It is clear that part of the rMS continues into SGB Group A (red line). Also MS-a is clearly connected with SGB Group D (green line). By contrast, the bMS can be followed only up to the TO (blue line), then it spreads into the SGB region.

Section 2.1. Eight of the WFI stars were eliminated from our list because their radial velocity was not compatible with the cluster velocity and we therefore considered them to be field stars. The coordinates of our final targets are reported in Col. 2 and 3 of Table 1 (*HST* sample), and Table 3 (WFI sample). Note that the center of the cluster (which can be used for radial distance determination of the target stars) is at $\alpha = 201^{\circ}691208$, $\delta = -47^{\circ}476861$.

The data were reduced using GIRAFFE pipeline 1.12 (Blecha et al. 2000), which corrects the spectra for bias and flat-field. (See <http://girbldrs.sourceforge.net> for documentation on the GIRAFFE pipeline and software.) Then each spectrum was corrected for its fiber transmission coefficient, which was found from five flat-field images, by measuring for each fiber the average flux relative to a reference fiber. A sky correction was applied to each stellar spectrum by subtracting the average of ten sky spectra

that were observed simultaneously with the stars (same FLAMES plate). The wavelength calibration uses both prior and simultaneous calibration-lamp spectra. Finally, each spectrum was normalized to the continuum, i.e., divided by a low-order polynomial that fits its continuum. The resulting spectra have a dispersion of $0.2 \text{ \AA}/\text{pixel}$ and a typical $S/N \sim 100\text{--}150$.

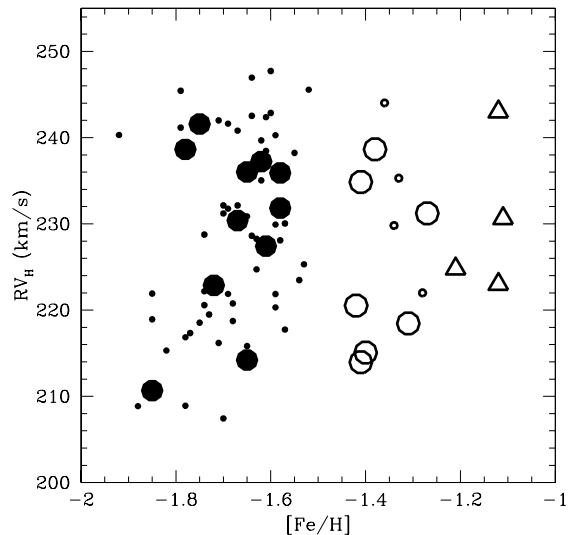


Fig. 7.— Heliocentric radial velocities of the observed stars vs. metallicity. Large symbols are *HST* stars, while small ones are WFI stars. Open triangles are the stars with SGB-a metallicity. Filled and open circles are SGB-MP and SGB-MInt2, respectively. (See Sect. 5 for definitions of the metallicity groups.)

We used the `gyCrossC.py` utility of the GIRAFFE pipeline to measure the radial velocity, which we then converted to heliocentric. The resulting velocities for the member stars (RV_H) are given in Tables 1 and 3, and shown in Fig. 7, where we plot radial velocity vs. metallicity. (See Sect. 5 for definitions of the metallicity groups.) In this figure and in a number of others, we distinguish between the *HST* sample (large symbols) and the WFI sample (small symbols), because they are at different distances from the center of the cluster, and later studies might want to make this distinction. The error in radial velocity is typically about $2\text{--}3 \text{ km/s}$. All the stars have the same radial velocity within $\pm 20 \text{ km/s}$. Considering the mean

radial velocity of ω Cen (~ 232 km/s, Reijns et al. 2006), the velocity dispersion in the inner part of the cluster (~ 15 km/s, Reijns et al. 2006) and the observational errors, all of the stars in Fig. 7 appear to be cluster members.

5. Terminology

At this point it is appropriate to consider what terminology we should use to identify the different populations of ω Cen.

As the number of sequences recognized in the CMD of ω Cen has increased, the number of designations for them has increased even faster. For the SGB, a useful terminology was introduced by Sollima et al. (2005a), who, by analogy with their terminology for the RGB (Sollima et al. 2005b), referred to the most metal-poor, most luminous of the subgiant branches as SGB-MP, the less luminous, less metal-poor subgiant region, with two populations, as SGB-Mint n (where n is 2 or 3), and the anomalous, apparently detached, faintest subgiant branch as SGB-a.

It is tempting to continue to use the same suffixes to identify the different SGBs, but the problem has become more complicated, because a new distinction must now be made. Whereas previous authors have referred to populations either by their metallicities or by locations in the color-magnitude diagram, in the present paper we will be showing that these two types of population criterion are not equivalent. It is therefore important that our terminology distinguish between them. What we will do here is to continue to refer to metallicity groups by the suffixes introduced by Sollima et al., but to introduce also, where necessary, new terms to distinguish populations according only to their locations in the CMD.

We will therefore use the suffixes -MP and -Mint2 only to designate stars whose $[\text{Fe}/\text{H}]$ values correspond approximately to those of the corresponding SGB metallicity groups of Sollima et al. (2005a). (Our sample does not happen to include any stars that belong to the Sollima et al. SGB-Mint3 group.) For sequences that have been identified photometrically, we use terms such as ‘‘SGB Group A’’. In the case of populations for which we use the suffix -a, however, we do not make a distinction, because at present neither their mean metallicity nor their metallicity dispersion is clear.

When we use the labels A, B, C, and D for groups in the SGB region, we should make it clear that these are arbitrary letters chosen for convenience and are not meant to imply that these are the only branches that will ever be distinguished. We also wish to make it abundantly clear that our designations within the CMD are meant for a particular region, such as MS, SGB, or RGB, and that the connections between such pieces are not necessarily known yet (see also Section 9 for a discussion).

6. Abundance measurements

In this Section we derive the Fe, C, N, Ca, Ti, and Ba abundances for the 22 stars from the *HST* fields, and the Fe abundances for the 58 stars selected from the WFI field. The measurement of Fe for the WFI stars is important in order to have a larger sample of stars for the estimates of relative ages that we will make in Sect. 9. The abundances of other elements for the WFI stars, however, are of less importance in the present paper, and will be presented in a future one.

For the stars in the *HST* field (Table 1), we derived effective temperatures (T_{eff}) from the $m_{\text{F435W}} - m_{\text{F625W}}$ color in the *HST* CMD. The relation between color and T_{eff} , as a function of $[\text{M}/\text{H}]$ (by which we mean the global metallicity, including alpha enhancement), was derived from isochrones by Pietrinferni et al. (2004, 2006). Colors were de-reddened using the absorption coefficients listed in Table 3 of Bedin et al. (2005), adopting $E(B-V) = 0.115$. As a first guess for the $[\text{M}/\text{H}]$ to be used in the color- $[\text{M}/\text{H}]$ -temperature relation, we adopted $[\text{Fe}/\text{H}] = -1.5$, the mean metallicity of ω Cen stars, along with an alpha enhancement of 0.3 dex; this enhancement is confirmed *a posteriori* by our abundance results. The $[\text{M}/\text{H}]$ was derived from the adopted $[\text{Fe}/\text{H}]$ and the alpha enhancement from the prescription by Salaris et al. (1993), along with the corresponding T_{eff} from the color- $[\text{M}/\text{H}]$ -temperature relation. Using this value for T_{eff} , we calculated $\log g$ and v_t and measured a new $[\text{Fe}/\text{H}]$ abundance as described below. Then for each star the values of T_{eff} and $[\text{Fe}/\text{H}]$ were changed in an iterative process, till convergence (when $\log g$ and v_t no longer change by a significant amount).

We estimated the effect of variations in helium

TABLE 1
HST STARS

ID	R.A.(J2000.0)	Decl.(J2000.0)	m_{F435W}	$m_{F435W} - m_{F625W}$	V	$RV_H(\text{km/s})$	$T_{\text{eff}}(K)$	$\log g$
3735	201.589019	-47.535167	18.08	1.07	17.38	214	5650	3.7
5533	201.584075	-47.488143	18.08	1.08	17.50	237	5670	3.8
7843	201.593368	-47.504161	18.06	1.09	17.39	236	5630	3.8
8756	201.607391	-47.560226	18.07	1.05	17.29	210	5680	3.8
13633	201.611114	-47.525005	18.42	1.12	17.63	238	5500	3.9
145	201.576721	-47.541572	18.04	1.08	17.26	222	5630	3.7
1472	201.565170	-47.455718	18.08	1.13	17.35	235	5540	3.7
2550	201.573867	-47.480480	18.32	1.15	17.64	238	5540	3.8
26656	201.641036	-47.551818	18.39	1.05	17.62	214	5760	4.0
299	201.557098	-47.442539	18.14	1.09	17.33	231	5680	3.7
3004	201.587936	-47.540699	18.36	1.04	17.66	227	5740	3.9
35208	201.653244	-47.554779	18.21	1.16	17.43	241	5430	3.8
3976	201.575729	-47.468921	18.31	1.10	17.68	218	5660	3.8
4079	201.595642	-47.561798	18.42	1.10	17.63	234	5660	4.0
4434	201.575195	-47.460380	18.26	1.04	17.65	215	5780	3.9
59481	201.680511	-47.552825	18.34	1.10	17.62	230	5600	3.9
63840	201.684097	-47.550704	18.29	1.09	17.60	231	5630	3.9
9462	201.608245	-47.556041	18.27	1.13	17.42	220	5580	3.8
6808	201.593612	-47.517513	18.15	1.02	17.46	230	5840	3.9
28448	201.642211	-47.545017	19.00	1.24	18.22	243	5400	4.1
5654	201.596649	-47.545948	19.01	1.25	18.02	224	5350	4.0
6766	201.591690	-47.508903	18.97	1.16	18.24	223	5550	3.9

content and age on the relation between color and temperature, as follows. Using the same set of isochrones, we found that a variation $\Delta Y = \pm 0.1$ in He content, and a $\Delta(\text{age}) = \pm 2$ Gyr each imply a variation of ~ 10 K in temperature for SGB stars, which translates into a change of ~ 0.01 dex in metallicity. Such small changes can be neglected.

The gravity $\log g$ was calculated from the elementary formula

$$\log\left(\frac{g}{g_{\odot}}\right) = \log\left(\frac{M}{M_{\odot}}\right) + 4 \log\left(\frac{T_{\text{eff}}}{T_{\odot}}\right) - \log\left(\frac{L}{L_{\odot}}\right).$$

The mass M/M_{\odot} was derived from the relations of Straižys & Kuriliene (1981) for the given T_{eff} , adopting a luminosity class IV for all the stars. (Even though these relations were derived for Population I stars, using them for Population II stars produces a negligible error in gravity.) The luminosity L/L_{\odot} was derived from the apparent magnitude V measured in WFI images, assuming the absolute distance modulus $(m - M)_0 = 13.75$ found by van de Ven et al. (2006), and the reddening adopted above. The bolometric correction (BC) was derived from the BC- T_{eff} relation of Alonso et al. (1999). Finally, the microturbulent velocity came from the relation (Houdashelt et al. 2000)

$$v_t = 2.22 - 0.322 \log g.$$

For all the stars we found $v_t \sim 1$ km/s.

For the stars in the WFI field, effective temperatures were the mean values of the temperatures derived from the color-[Fe/H]-temperature relations of Alonso et al. (1996), Alonso et al. (1999), and Sekiguchi & Fukugita (2000), using the de-reddened $B - V$, $V - I_C$, and $V - R_C$ colors. The $\log g$ and v_t parameters were obtained as for the *HST* stars. The adopted atmospheric T_{eff} and $\log g$ are listed in Tables 1 and 3 for the *HST* and WFI stars, respectively.

Since our scales of effective temperature were derived in different ways for the two different sets of targets (*HST* and WFI), we verified that they agree with each other. To this purpose, we measured the temperatures of the *HST* stars following the same procedure that was used for the WFI targets, i.e., using their WFI B , V , R_C , and I_C magnitudes, and the color-temperature relations of Alonso et al. (1996), Alonso et al. (1999), and Sekiguchi & Fukugita (2000), in order to derive an independent value of T_{eff} . We obtained temperatures which differ, on average, by less than 10 K from the T_{eff} values that we had determined using the *HST* photometry and the Pietrinferni et al. isochrones.

The agreement between temperature scales implies that our adopted color-temperature relations

are consistent with each other. We therefore expect that systematic differences between our metal abundances and those derived by others from these color-temperature relations and Kurucz model atmospheres will be negligible.

On the other hand, our absolute metal abundances could have systematic errors of the order of 0.15–0.20 dex, because of systematic errors in effective temperatures, and uncertainties in model atmospheres and in reddening.

The metal content was obtained by comparison with synthetic spectra calculated using SPECTRUM, the local-thermodynamical-equilibrium spectral synthesis program freely distributed by Richard O. Gray. (See www.phys.appstate.edu/spectrum/spectrum.html for more details.) The model atmospheres of Kurucz (1992), used throughout this paper, assume $N_{\text{He}}/N_{\text{H}} = 0.1$, corresponding to $Y = 0.28$ by mass. The bMS and, quite reasonably, the related SGB stars (i.e., stars with the same metallicity as the bMS stars), were assumed to have a helium content $Y \sim 0.38$, in accordance with our assumption that the bMS stars are helium-rich. As discussed in P05, this increase in helium introduces an error smaller than 0.03 dex in the metal-abundance determinations, which is negligible. We firstly measured a metallicity index $[A/H]$, as in P05. This index comes mainly from Fe lines, plus some lines of α -elements like Ca and Ti. (See P05 for its exact definition.) We chose this index because it is the metallicity index used by P05, and we wanted to compare the results of this paper with the results of P05. They had to resort to $[A/H]$ (and not $[\text{Fe}/\text{H}]$, as we will do in the present paper) because of the lower S/N of their spectra. P05 called their metallicity index $[M/H]$; here we prefer to use a different name in order to avoid confusion with the symbol $[M/H]$ that is commonly used for global metallicity, as we did above.

Our $[A/H]$ values were obtained from a comparison of each observed spectrum with five synthetic ones (see Fig. 8), calculated with different metal abundances but with other element ratios as in the Sun. We normalized these spectra to the continuum, as we did for the observed spectra. The comparison was done in the 4400–4450 Å interval, because this region contains numerous metal lines (mainly due to Fe-peak elements, with a few strong Ca and Ti lines) but has few lines

due to molecules (CH and CN), and no strong H lines. The synthetic spectra were smoothed to the resolution of the observed spectra.

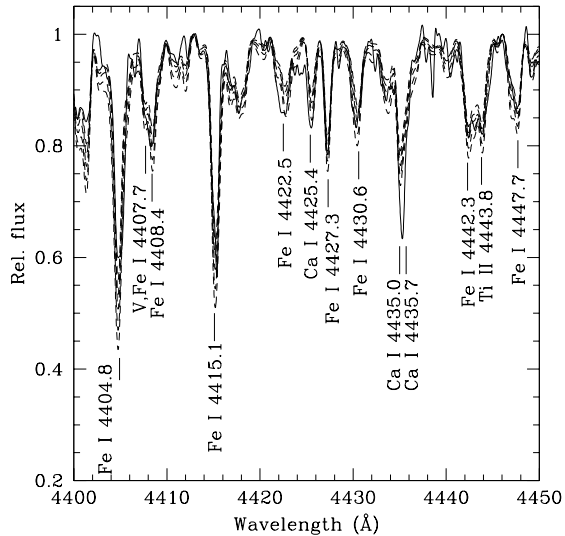


Fig. 8.— The spectrum of star 28448 in the wavelength interval 4400–4450 Å (continuous line). Superposed are the synthetic spectra for metallicities $[\text{Fe}/\text{H}]$ -1.4 , -1.2 , -1.0 , -0.8 , -0.6 (dashed lines). Many spectral lines are identified.

The metallicity was obtained by two different methods. The first one is the method used by P05: their $[A/H]$ is the value that minimizes the r.m.s. scatter of the differences between the observed and synthetic spectra (as illustrated in the upper panel of Fig. 9). In the second method, we measured an equivalent width (EW) for the whole 4400–4450 Å region. The EW of the observed spectrum (EW_{obs}) was then divided by the EWs of the theoretical ones (EW_{synth}), and an empirical relation was derived between $\text{EW}_{\text{obs}}/\text{EW}_{\text{synth}}$ and $[A/H]$ (as shown in the lower panel of Fig. 9). The resulting $[A/H]$ is the value that corresponds to $\text{EW}_{\text{obs}}/\text{EW}_{\text{synth}} = 1$, as obtained from interpolation in the empirical relation. We have verified that the metallicities obtained in these two ways agree within 0.05 dex, allowing us to estimate that the error due to the methods is less than 0.03 dex. The final adopted metallicity is the average of the values from the two methods. As a test of our methodology, we used a solar spectrum from the ESO archive (<http://archive.eso.org/>), obtained

TABLE 2
ABUNDANCES AND AGES FOR THE *HST* STARS.

ID	[A/H]	[Fe/H]	[C/Fe]	[N/Fe]	[Ca/Fe]	[Ti/Fe]	[Ba/Fe]	Age
3735	-1.64	-1.76	0.13	1.16	0.35	0.44	0.95	0.63
5533	-1.55	-1.62	0.00	1.06	0.55	0.41	1.11	0.64
7843	-1.57	-1.65	0.00	1.33	0.37	0.34	0.97	0.63
8756	-1.62	-1.85	0.03	1.11	0.17	0.36	0.71	0.59
13633	-1.64	-1.78	0.03	1.62	0.32	0.25	1.00	0.94
145	-1.61	-1.72	0.06	1.49	0.43	0.37	0.62	0.61
1472	-1.54	-1.58	0.35	1.07	0.33	0.24	0.73	0.69
2550	-1.27	-1.38	-0.05	1.48	0.42	0.43	0.88	0.79
26656	-1.28	-1.41	-0.07	1.61	0.44	0.39	0.85	0.83
299	-1.21	-1.27	0.12	1.67	0.60	0.30	1.03	0.85
3004	-1.55	-1.61	0.23	1.30	0.34	0.33	0.65	0.77
35208	-1.64	-1.75	0.08	0.93	0.27	0.31	0.60	0.71
3976	-1.24	-1.31	-0.09	1.59	0.36	0.41	1.06	0.59
4079	-1.29	-1.41	-0.13	1.67	0.26	0.36	1.00	0.72
4434	-1.27	-1.40	0.00	1.73	0.32	0.28	1.01	0.78
59481	-1.57	-1.67	-0.01	1.58	0.42	0.37	0.82	0.62
63840	-1.31	-1.48	-0.20	1.55	0.33	0.26	0.99	0.68
9462	-1.32	-1.42	-0.22	1.44	0.43	0.24	0.85	0.72
6808	-1.03	-1.11	-0.18	1.72	0.41	0.49	0.94	0.64
28448	-1.02	-1.12	-0.18	1.73	0.55	0.30	0.99	1.01
5654	-1.05	-1.21	0.00	1.70	0.46	0.56	1.03	1.01
6766	-1.01	-1.12	0.03	1.67	0.52	0.41	1.06	0.98

with the same instrument and the same configuration (FLAMES@VLT+GIRAFFE, LR2 mode), and we calculated a synthetic spectrum for the Sun using the canonical solar atmospheric parameters ($T_{\text{eff}} = 5777 \text{ K}$, $\log g = 4.44$, $v_t = 0.8$). We verified that our procedure (i.e., the program, the model atmosphere, and the line list used) reproduces the strengths of the solar spectral features. For this purpose we measured the abundances of the Sun for the elements considered in this paper by the same method used for the target stars. We obtained: $[\text{Fe}/\text{H}] = -0.02$, $[\text{C}/\text{Fe}] = -0.10$, $[\text{N}/\text{Fe}] = +0.08$, $[\text{Ca}/\text{Fe}] = +0.05$, $[\text{Ti}/\text{Fe}] = -0.07$, $[\text{Ba}/\text{Fe}] = +0.10$. We conclude that our procedure reproduces the solar values well, within 0.10 dex.

For the measurement of the $[\text{Fe}/\text{H}]$ value we applied the same methods, but restricted the comparison of the observed and theoretical spectra to the 4400–4425 Å region, which contains only iron lines. The smaller spectral interval, with fewer spectral lines, implies a larger error in the final metallicity. The mean difference between $[\text{A}/\text{H}]$ and $[\text{Fe}/\text{H}]$ is 0.11 dex (useful for comparing the results of this paper with P05), with $[\text{A}/\text{H}]$ higher than $[\text{Fe}/\text{H}]$, as expected because of the α -enhancement. The $[\text{A}/\text{H}]$ and $[\text{Fe}/\text{H}]$ values derived for the 22 *HST* stars are listed in Table 2, while Table 3 gives the $[\text{Fe}/\text{H}]$ abundances ob-

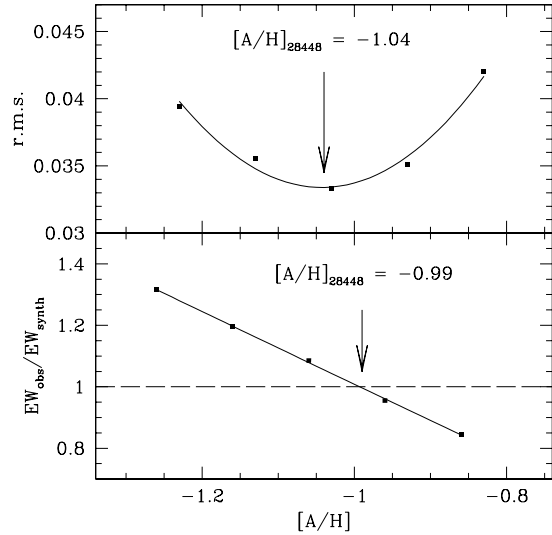


Fig. 9.— The r.m.s. scatter (upper panel), and the empirical relation between $[\text{A}/\text{H}]$ and $\text{EQW}_{\text{obs}}/\text{EQW}_{\text{synth}}$ (lower panel), for star 28448. The metal abundance of the star is given by the minimum value of the r.m.s. curve (first method) and by the $[\text{Fe}/\text{H}]$ value corresponding to $\text{EQW}_{\text{obs}}/\text{EQW}_{\text{synth}} = 1$ (second method).

tained for the 58 WFI stars. As explained above,

no measurement of $[A/H]$ was made for the WFI stars.

We found the accidental error in $[A/H]$ from the distribution of differences between the values derived from equal halves of our wavelength range; typical errors for the whole range are 0.04–0.05 dex. Typical errors for $[Fe/H]$ should be 0.06–0.07, since $[Fe/H]$ is obtained from a spectral region only half as long. To these errors we should add (in quadrature) the error due to photometric uncertainty in the colors; the error in color is typically of the order of 0.01 magnitude, which translates into a 0.02 dex error in abundance. After allowing also for the error that comes from the uncertainty in the He content (less than 0.03 dex, as we have shown in P05), we adopt an overall uncertainty of 0.06 dex for $[A/H]$ and 0.08 dex for $[Fe/H]$. This is the internal error in our metallicity measurement. In addition there can be a systematic error of the order of 0.15–0.20 dex, because of systematic uncertainties in effective temperatures, and uncertainties in model atmospheres and in reddening. The systematic errors do not affect the relative metallicities of the different stellar populations of ω Cen that we will discuss in later sections.

As a final test, we considered the possible contamination of the spectra by close neighboring stars. This problem might affect the metallicity measurement of the *HST* targets, which are all near the rather crowded center; all WFI targets are located in much less crowded outer regions. In the *HST* images, we measured instrumental magnitudes of the target stars and the neighbors, and their separations. In order to minimize contamination, the choice of stars for targeting had not allowed any star with a neighbor that is closer than 2.4 arcsec (twice the diameter of a fiber) and is fainter by less than 2 magnitudes. There is, in fact, one neighbor 0.6 arcsec from a target star, but it is ~ 2.5 magnitudes fainter. For this worst case we calculated synthetic spectra for the neighbor and for the target star, assuming as worst-case metallicities $[Fe/H] = -1.7$ for the target star and $[Fe/H] = -1.1$ for the neighbor. We summed the two spectra, weighting for the magnitude difference and for the flux captured by the fiber, and derived a metallicity $[A/H]$; the result differed by less than 0.03 dex from the metallicity of the target star.

In addition to $[Fe/H]$, we were also interested in

the abundances of other elements. We have been able to measure the abundances of C, N, Ca, Ti, and Ba for the 22 *HST* stars. Calcium, titanium, and barium abundances were obtained from the spectral lines of Ca I at 4435 Å (Fig. 10), Ti II at 4468 Å (Fig. 11), and Ba II at 4454 Å (Fig. 12). Carbon abundances were obtained by comparing the observed spectra with synthetic ones in the spectral region 4300–4330 Å (see Fig. 13), which includes the $\Delta v = 0$ strong band heads of the $A^2\Delta - X^2\Pi$ transition of CH, computed with appropriate model-atmosphere parameters, and different values of the C abundances. Nitrogen abundances were found by a similar comparison for the region 4200–4225 Å (see Fig. 14), which includes the $\Delta v = -1$ band heads of the $X^2\Sigma - B^2\Sigma$ CN transition. All the abundances are listed in Table 2.

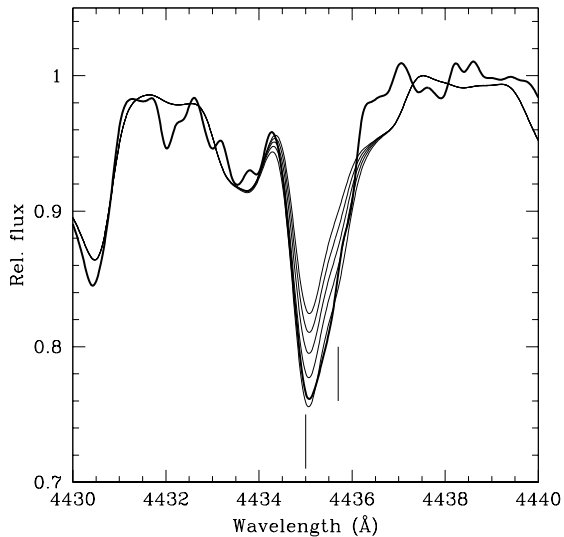


Fig. 10.— The spectrum of the star 6766, compared with synthetic spectra in the region 4430–4440 Å, which includes the Ca I lines at 4435.0 and 4435.7 Å. (Their locations are marked.) Synthetic spectra were computed for Ca abundances $[Ca/Fe] = -0.2, 0.0, +0.2, +0.4, +0.6$ dex. Thick line is the observed spectrum; thin lines are the synthetic spectra.

An upper limit for the errors in C, N, Ca, Ti, and Ba content was calculated by assuming that the abundances of these elements are the same within the intermediate-metallicity popula-

tion (SGB-MInt2) and within the metal-rich population (SGB-a), and calculating the average r.m.s. spread of the measured abundance distributions of these five elements. (See Sect. 5 for definitions of these populations.) The final error is ~ 0.1 dex. This error should be considered an overestimate of the uncertainties in the C, N, Ca, Ti, and Ba abundances, because of the possibility of an intrinsic dispersion for these elements among the measured stars. In any case, we cannot do better, because the abundances were obtained from a spectral interval that is too small (too few lines) for us to apply the compare-two-halves method that was used to estimate the uncertainty in $[A/H]$.

7. Discussion of the spectroscopic results

Figure 15 shows the histogram of the $[\text{Fe}/\text{H}]$ distribution of all our target stars. (Because of the small number of stars observed, and the selection biases, the figure cannot be construed as showing the quantitative metallicity distribution of ω Cen

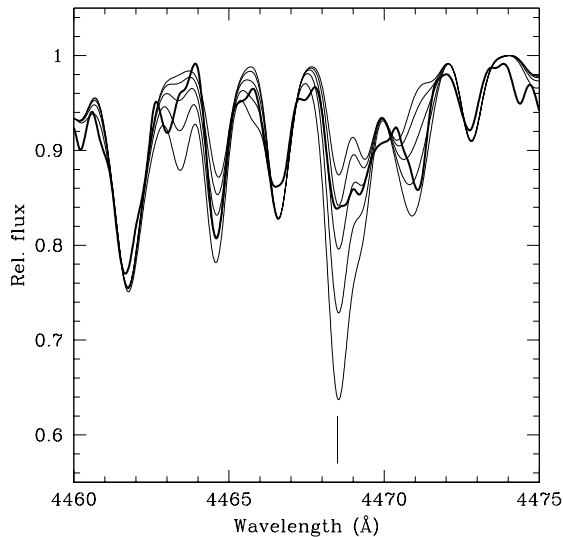


Fig. 11.— The spectrum of the star 28448, compared with synthetic spectra in the region 4460–4475 Å, which includes the Ti II line at 4468.5 Å. (The location of the line is marked.) Synthetic spectra were computed for Ti abundances $[\text{Ti}/\text{Fe}] = -0.6, -0.2, +0.2, +0.6, +1.0$ dex. Thick line is the observed spectrum; thin lines are the synthetic spectra.

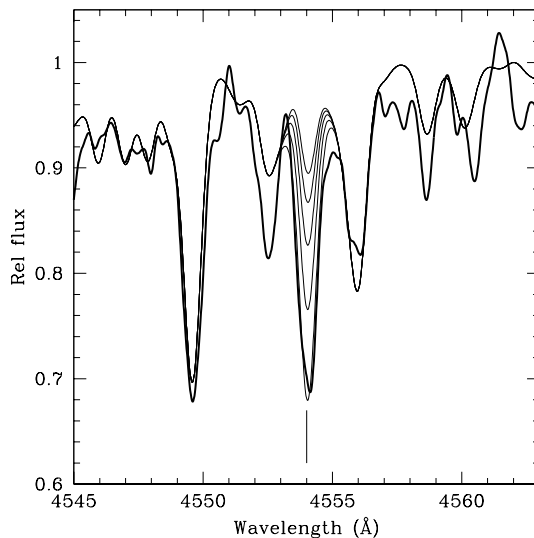


Fig. 12.— The spectrum of the star 5654, compared with synthetic spectra in the region 4545–4563 Å, which includes the Ba II resonance line at 4554 Å. (The location of the line is marked.) Synthetic spectra were computed for Ba abundances $[\text{Ba}/\text{Fe}] = -0.6, -0.2, +0.2, +0.6, +1.0$ dex. Thick line is the observed spectrum; thin lines are the synthetic spectra.

stars, but it does give the shape of the distribution). In the figure we can distinguish three groups of stars, whose average metallicities are in agreement with three of the four metallicity groups in the recent spectroscopic survey of SGB stars in ω Cen by S05, who found four populations running through the SGB region. We can identify our peak at $[\text{Fe}/\text{H}] \sim -1.7$ with their SGB-MP and our peak at $[\text{Fe}/\text{H}] \sim -1.4$ with their SGB-MInt2. [We omit the Mint1 of the Sollima et al. (2005b) photometric paper that deals only with the RGB, as it does not appear in their spectroscopic paper (2005a = S05) on the SGB. Also, our sample does not include any stars in the part of the CMD where they identify a fourth component, which they call SGB-MInt3.] Our peak at $[\text{Fe}/\text{H}] \sim -1.1$ can be identified with their SGB-a.

The SGB-a group needs some further comments. There is no doubt that as defined by S05 (see their Fig. 1), this is the faintest SGB, corresponding to our SGB Group D. Therefore SGB-a is

well identified, at least from the photometric point of view. However, it is not at all clear why S05 assign a metallicity $[\text{Fe}/\text{H}] = -0.6$ to this group of stars. Indeed, panel *d* of their Fig. 4 shows that the SGB-a stars in their sample have a double-peaked metallicity distribution, with one peak at $[\text{Fe}/\text{H}] \sim -1.0$ (as confirmed by our observations), and a second one at $[\text{Fe}/\text{H}] \sim -0.6$. Unlike S05, in our survey we have not identified any stars with $[\text{Fe}/\text{H}] \sim -0.6$, but their absence may be due to the small number of SGB-a stars that we observed. On the other hand, Pancino et al. (2002) found $\langle [\text{Fe}/\text{H}] \rangle \sim -0.6 \pm 0.15$ from high-resolution spectroscopy of three stars on RGB-a (which appears to be the continuation of SGB-a on the RGB), confirming the presence in this sequence of a population with a metallicity as high as $[\text{Fe}/\text{H}] = -0.6$.

The dispersion of the stars of SGB-a in the CMD (as shown in Figs. 4 and 5) is clearly not consistent with as broad a dispersion in the metal content of the SGB-a stars as was found by S05. To show this we compared two isochrones from

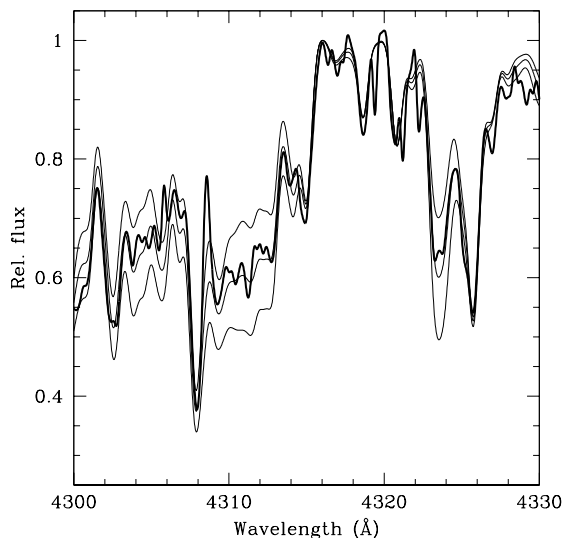


Fig. 13.— The spectrum of the star 5654, compared with synthetic spectra in the region 4300–4330 Å, which includes the CH band head. Synthetic spectra were computed for C abundances $[\text{C}/\text{Fe}] = -0.2, 0.0, +0.2$ dex. Thick line is the observed spectrum; thin lines are the synthetic spectra.

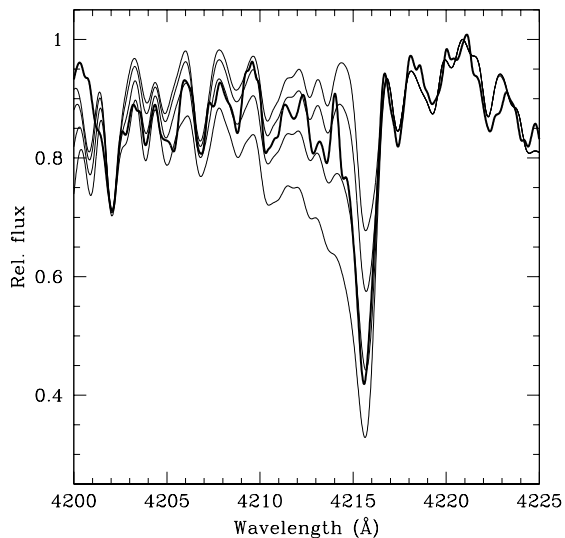


Fig. 14.— The spectrum of the star 6766, compared with synthetic spectra in the region 4200–4225 Å, which includes the band heads of the $\Delta v = 2-0$ violet CN band. The synthetic spectra were computed for appropriate C content and for N abundances $[\text{N}/\text{Fe}] = +1.0, +1.4, +1.8, +2.0$ dex. Thick line is observed spectrum; thin lines are synthetic spectra.

Pietrinferni et al. (2004, 2006), having the same age but with $[\text{Fe}/\text{H}] = -1.1$ and $[\text{Fe}/\text{H}] = -0.6$, respectively. Their separation in magnitude is more than twice as large as the magnitude dispersion actually observed in SGB-a. One possible explanation for the large metallicity spread in the SGB-a sample of S05 is that their $[\text{Fe}/\text{H}]$ estimates are based on the Ca II triplet. Such measurements are subject to large errors, because the relation between the equivalent width of the Ca II triplet and $[\text{Fe}/\text{H}]$ depends strongly on the gravity (which corresponds to luminosity). S05 noted that they needed to calibrate this relation, but the catalog of reference spectra that they used includes very few stars in the appropriate ranges of temperature and gravity. Their SGB-a sample spans more than a magnitude in *R*; it is not out of the question that such a large magnitude spread could be at least partially responsible for the large metallicity dispersion that they find for the SGB-a stars.

To complicate the scenario further, the referee has noted that Norris & Da Costa (1995) found

a group of RGB stars with $[\text{Fe}/\text{H}] \sim -1.1$, which are apparently not present in RGB-a. This means that in the RGB region there are two groups of stars, one with $[\text{Fe}/\text{H}] \sim -1.1$, and a second with $[\text{Fe}/\text{H}] \sim -0.6$. The former could be the progeny of our SGB-a stars.

In short, we believe that the problem of the metal content of the SGB-a stars and of a possible dispersion in it, and the problem of the connection of the SGB-a sequence with the RGB-a of Pancino et al. (2000), and with the RGB in general, are both still open, and require further investigation.

7.1. Comparison with P05

In order better to understand the connection between the multiple SGBs in ω Cen and the multiple MSs, it is useful to compare the results presented in this paper with those of P05. There it was found that $[\text{A}/\text{H}] = -1.57$ for the rMS and $[\text{A}/\text{H}] = -1.26$ for the bMS; when we apply the

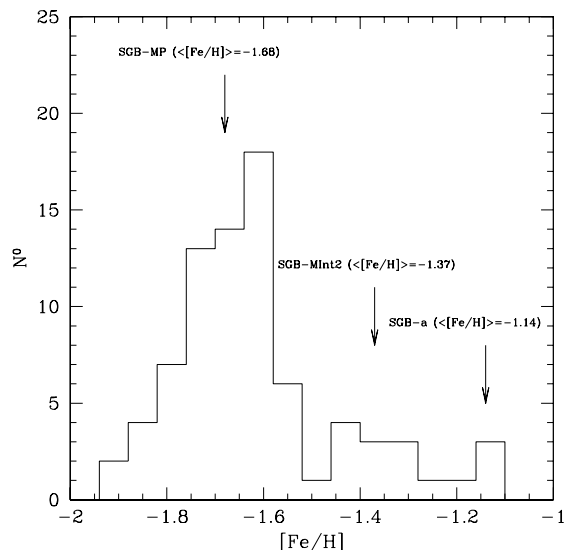


Fig. 15.— Histogram of the metallicity distribution of the target stars. Three peaks are present. The first (SGB-MP), at $[\text{Fe}/\text{H}] \sim -1.7$, has the same average metallicity as the rMS of B04, and corresponds to the bulk of the RGB population. The second one (SGB-MInt2), at $[\text{Fe}/\text{H}] \sim -1.4$, has the same average metallicity as the bMS. The third one, at $[\text{Fe}/\text{H}] \sim -1.1$, corresponds to the SGB-a population.

0.11 dex correction needed to transform $[\text{A}/\text{H}]$ into $[\text{Fe}/\text{H}]$, as described in Sect. 6, these values correspond respectively to $[\text{Fe}/\text{H}] = -1.68$ and $[\text{Fe}/\text{H}] = -1.37$. In the present paper we found for the SGB-MP stars a mean $[\text{Fe}/\text{H}]$ of -1.68 dex, and for the SGB-MInt2 stars a mean $[\text{Fe}/\text{H}]$ of -1.37 dex. At this point, on the basis of the metallicity measurements available, it is very tempting to identify the SGB-MP stars as the progeny of the rMS stars, and the SGB-MInt2 stars as the progeny of the bMS stars. We will return to this question in later sections.

In P05 we determined the abundances of C, N, and Ba. Here, in addition to those we have extended our analysis to include the α -elements Ca and Ti. Figure 16 shows the trend of the abundance ratios as a function of $[\text{Fe}/\text{H}]$. Our measured abundances of C, N, and Ba for SGB stars are in good agreement with the results of P05 for the MS. In P05, for both branches of the MS we found $[\text{C}/\text{A}] \sim 0$, corresponding to $[\text{C}/\text{Fe}] \sim 0.1$ after application of the 0.11 dex correction to transform the $[\text{A}/\text{H}]$ into $[\text{Fe}/\text{H}]$, as discussed in Section 6; here, for metal-poor stars (the filled circles in Fig. 16) $[\text{C}/\text{Fe}]$ spreads from -0.1 to $+0.4$ dex, while for intermediate-metallicity stars (the open circles in Fig. 16) $[\text{C}/\text{Fe}]$ runs from -0.3 to 0.1 dex. As for the nitrogen content, in P05 we found for the rMS $[\text{N}/\text{A}] \leq 1.0$ ($[\text{N}/\text{Fe}] \leq 1.1$ after applying the 0.11 dex correction), and $[\text{N}/\text{A}] \sim 1.0$ – 1.5 ($[\text{N}/\text{Fe}] \sim 1.1$ – 1.6) for the bMS; here, for metal-poor stars (corresponding to the rMS) $[\text{N}/\text{Fe}]$ spreads over a range from $+0.9$ to $+1.6$ dex, while for intermediate-metallicity stars (corresponding to the bMS) N spreads over a range from $+1.4$ to $+1.7$ dex. In summary, for low metallicities ($[\text{Fe}/\text{H}] \sim -1.7$) the mean abundances of C and N are $[\text{C}/\text{Fe}] \sim 0.1$ and $[\text{N}/\text{Fe}] \sim 1.3$, respectively, while when the metallicity increases $[\text{C}/\text{Fe}]$ decreases to ~ -0.1 and $[\text{N}/\text{Fe}]$ increases to ~ 1.6 – 1.7 . Compared with the MS stars, SGB stars have slightly lower C abundance, and higher N abundance.

Concerning Ba, in P05 we found $[\text{Ba}/\text{A}] \sim 0.4$ ($[\text{Ba}/\text{Fe}] \sim 0.5$) for the rMS and $[\text{Ba}/\text{A}] \sim 0.7$ ($[\text{Ba}/\text{Fe}] \sim 0.8$) for the bMS; here, for metal-poor stars $[\text{Ba}/\text{Fe}]$ spreads over a range from $+0.5$ to $+1.1$ dex, while for intermediate-metallicity stars $[\text{Ba}/\text{Fe}]$ spreads over a range from $+0.8$ to $+1.1$ dex. We note that metal-poor stars have a Ba

content lower than intermediate-metallicity ones by about 0.2 dex.

Finally, we analyzed the alpha elements. Both Ca and Ti show, in both metal-poor and intermediate-metallicity stars, the enhancement of about 0.3–0.4 dex that is typical of intermediate-metallicity globular clusters. SGB-a (the open triangles in Fig. 16) shows a chemical composition similar to the SGB-MInt2 populations, with a marginally greater (0.1 dex) excess of alpha elements: $[C/Fe] \sim -0.1$, $[N/Fe] \sim +1.7$, $[Ca/Fe] \sim +0.5$, $[Ti/Fe] \sim +0.4$, and $[Ba/Fe] \sim +1.0$.

As a final point, it is worth noting that the C and N content of the SGB-MInt2 population (as well as of the metal-rich one) is consistent with what is predicted by Maeder & Meynet (2006) for star-forming gas contaminated by the ejecta of fast-rotating metal-poor massive stars; most importantly, this could explain the very high He yield implied by the results of P05 (see Maeder & Meynet 2006 for further details).

7.2. Comparison with other investigations

The metallicity groups identified in Fig. 15 correspond to similar groups already identified on the RGB of ω Cen, and the average metallicity of all our SGB stars is in general agreement with the results of Suntzeff & Kraft (1996), Norris et al. (1996), Pancino et al. (2000), and Rey et al. (2004). In fact, these previous studies show the presence of at least three peaks in the metallicity distribution of the RGB stars of ω Cen, the first at $[Fe/H] \sim -1.7$ (corresponding our SGB-MP group), the second at $[Fe/H] \sim -1.4$ (corresponding to our SGB-MInt2), and the third at $[Fe/H] \sim -1.0$ (corresponding to our SGB-a).

It is useful to compare our results for the abundances of C, N, Ca, Ti, and Ba in SGB stars with those of Norris & Da Costa (1995, hereafter ND95) for the RGB stars, as ND95 present the most complete and extended results on the chemical composition of ω Cen. ND95 found a large spread in $[C/Fe]$, which spans the interval from -0.8 to $+0.2$ dex; the spread is clearly present in the entire metallicity range ($-1.8 < [Fe/H] < -0.8$) covered by the stars of their sample. We found $-0.2 < [C/Fe] < 0.4$, with a tendency for the most metal-poor stars to have a C content higher by ~ 0.2 dex. The offset between the C

abundances obtained in this paper and those of ND95 can be explained by the different evolutionary phase, since it is well known that stars brighter than the RGB bump (as are those observed by ND95) are depleted in C with respect to subgiants (see Gratton et al. 2000). As for the N content, the agreement is less satisfactory, though we must take note of the large errors (0.5 dex) of the ND95 measurements of N abundances. ND95 found a large spread in $[N/Fe]$, spanning the interval from 0.0 to 1.0 dex at every metallicity. On average, our $[N/Fe]$ values are larger by ~ 0.6 dex. (Also, ND95 notice that their mean $[N/Fe]$ value is 0.4–0.5 lower than in other work, e.g., Brown & Wallerstein 1993.)

We also find a large dispersion in $[N/Fe]$ for the SGB-MP, while at higher metallicity we have $[N/Fe] \sim 1.6$ with a small dispersion. There is good agreement between our study and ND95 when we consider Ca and Ti (both of them alpha elements). Both the present paper and ND95 find for the stars of ω Cen the alpha-element overabundance of about 0.3–0.4 dex that is typical of intermediate and metal-poor globular clusters. There is agreement between the Ba content measured in the present work and that of ND95, for the SGB-MP stars (with a small overabundance, by 0.1–0.2 dex, in our results), but at higher metallicity we have an overabundance of ~ 0.3 –0.4 dex with respect to ND95.

Another important contribution to knowledge of the chemical composition of ω Cen was made by Smith et al. (2000). In this case, our results agree well: Smith et al. found a Ca and Ti content between 0.2 and 0.4 dex, as we do; but, more interesting, the Ba abundance also agrees, with the bulk of stars in their paper having $[Ba/Fe]$ between 0.5 and 1.0 dex.

8. The structure of the subgiant branch

At this point it is very instructive to put together the results from the photometric and the spectroscopic investigations, in order better to characterize the structure of the SGB of ω Cen, the distribution of the stars along it, the properties of the stars in the different SGB groups, and the connection of the SGB sequences with those in the MS and RGB regions.

On the basis of the results of P05 on the metal

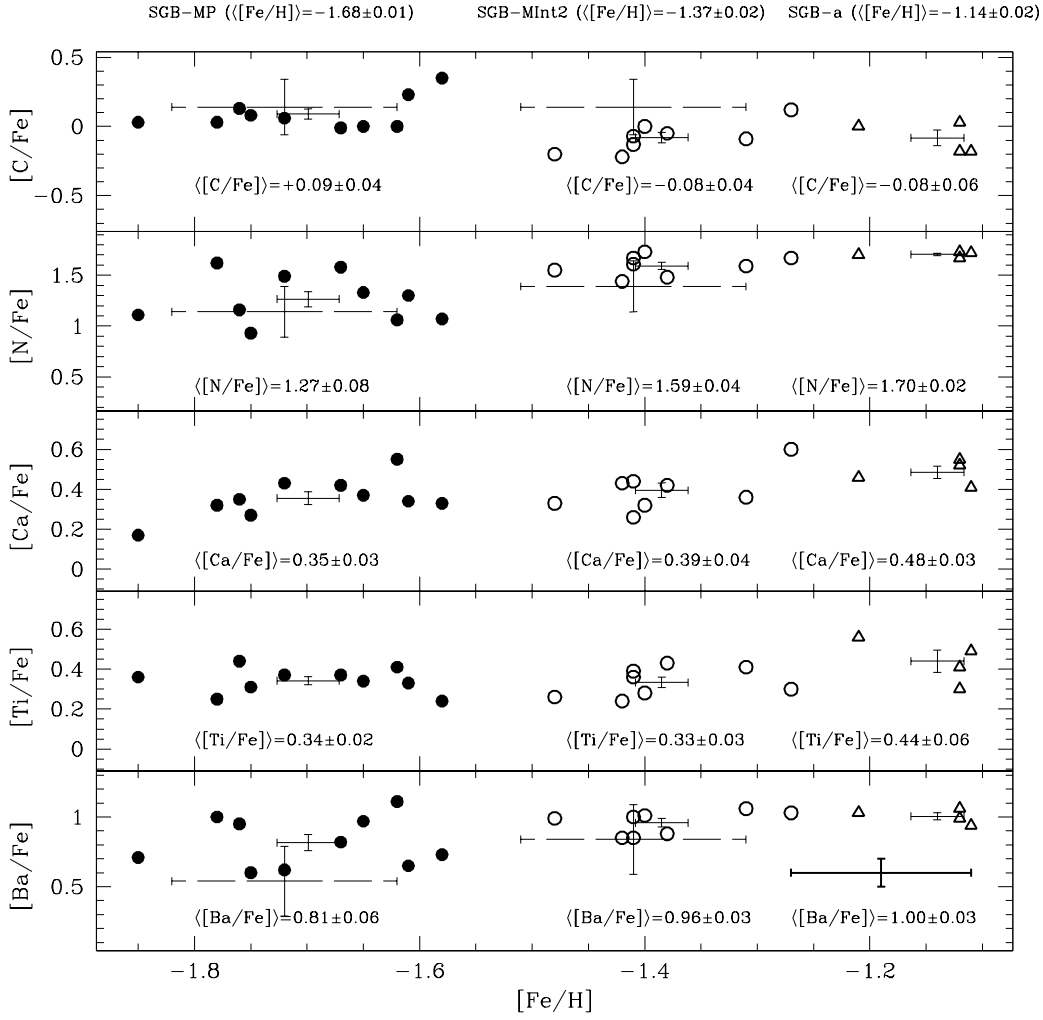


Fig. 16.— The C, N, Ca, Ti, and Ba abundances for the 22 *HST* stars. For each population the mean metallicity ($[\text{Fe}/\text{H}]$) is labeled at the top of the figure. For each element and each population we labeled and plotted the mean value of the abundances (continuous lines), with the error of the mean, and the results of P05, when available (dashed lines). The continuous thick line at the lower right shows the error for a single measure.

content of the two MSs in ω Cen, and of the metallicity measurements presented in the present paper, it seems appropriate to identify the SGB stars in the group that has $[\text{Fe}/\text{H}] \sim -1.7$ (SGB-MP) as the progeny of the RMS stars, and the SGB population that has $[\text{Fe}/\text{H}] \sim -1.4$ (SGB-MInt2) as the progeny of the bMS stars, as discussed in

Section 7.1.

In order to complete the observational scenario, Figs. 17 and 18 show the location in the CMD of the SGB stars whose metal content we have measured. Figure 17 is limited to the *HST* spectroscopic sample, and shows the CMD from the *HST* data. Figure 18 shows all of the target stars,

in a CMD that combines *HST* and WFI data. Note that our *HST* and WFI photometries have nearly the same accuracy; although in uncrowded regions our *HST* photometry tends to be more accurate than ground-based photometry, the *HST* fields used here are in the crowded central part of the cluster. Even so, the much larger *HST* sample gives better separation of the different SGB groups. From Figs. 17 and 18 we can conclude that:

- All of the stars in our sample that come from SGB Group A (which peaks at $X = 0$ in Fig. 4) are metal poor and fall within the SGB-MP metallicity group. As discussed in Section 7.1, the SGB-MP stars have the same metal content as the rMS stars. As suggested by the CMD of Fig. 6, the spectroscopic results confirm that the SGB stars of group A are probably the progeny of the rMS.
- The SGB-MP stars ($-1.90 \leq [\text{Fe}/\text{H}] \leq -1.50$) show a large magnitude dispersion, ~ 0.5 mag in m_{F435W} or B .
- None of our intermediate-metallicity SGB-MInt2 stars ($-1.50 \leq [\text{Fe}/\text{H}] \leq -1.25$) is located on SGB Group A; apparently, SGB-MInt2 stars are fainter ($X < -0.1$) than SGB Group A.
- The SGB-MInt2 stars also show a large dispersion in magnitude, though a smaller one than the SGB-MP stars: ~ 0.3 magnitude in m_{F435W} or B . As discussed in Section 7.1, the SGB-MInt2 stars have the same metal content as the bMS stars, and therefore at least part of them are likely to be the progeny of that sequence.
- The stars in the faintest SGB group, D (the peak at $X = -0.95$ in Fig. 4), all have $[\text{Fe}/\text{H}] \sim -1.1$.
- None of the stars in our sample, not even the three stars in SGB group D, have $[\text{Fe}/\text{H}] \sim -0.6$.
- There is one star (No. 6808) that has $[\text{Fe}/\text{H}] = -1.1$ (and therefore belongs to the SGB-a metallicity group) but is located in the uppermost SGB group, A, in the CMD. It is

marked in Fig. 17. It is well separated from any neighbors in the ACS field, and its photometric measurements pass all of the selection criteria that identify the stars with the best photometry in the ACS catalog. We consider its location in the CMD to be well established.

- Unfortunately, our sample contains no stars in the range $-0.80 < X < -0.45$ in Fig. 4 (which should correspond to the SGB-MInt3 group of S05).

With the help of the histogram in the lower panel of Fig. 4, and taking into account the conclusions just stated, we can make a rough estimate of the fraction of stars in each of the SGB populations. We began by fitting four Gaussians to the distribution of SGB stars shown in the lower panel of Fig. 4, centered at the four peaks marked in the histogram. We then integrated the areas under these Gaussians, and found that SGB Group A includes $\sim 33\%$ of the total stars, SGB Group B $\sim 29\%$, SGB Group C $\sim 20\%$, and SGB Group D (which corresponds to SGB-a) $\sim 10\%$ of the total SGB population. The remaining $\sim 8\%$ is distributed in the region corresponding to $-0.80 < X < -0.45$.

9. The Subpopulations of ω Cen

Before trying to understand the formation history of this intriguing cluster, we need to identify and characterize each of its discrete subpopulations. Individual subpopulations can be identified either photometrically, from position in the CMD, or spectroscopically, by metallicity. To complicate the issue, while such identifications can be made separately on the main branches of the CMD (MS, SGB, RGB, HB), for most cases in ω Centauri it is not obvious from the CMD alone how a population identified on a specific branch connects to those on other branches, and, in particular, which are the MS and RGB partners of a given SGB population.

On the MS we have three well-identified populations (see Figs. 2 and 3), which in Section 3.1 we called rMS, bMS, and MS-a. On the SGB there are four different sequences (see Figs. 4 and 5), which in Section 3.2 we called SGB Groups A, B, C, and D, and there is a hint of a fifth sequence

at a position intermediate between Groups C and D. The RGB has a very broad component, and a much redder component that is clearly detached. According to Sollima et al. (2005b) the RGB splits into five subcomponents, which they call RGB-MP, RGB-Mint1, RGB-Mint2, RGB-Mint3, and RGB-a, in order of increasing metallicity. While RGB-MP and RGB-a are well-established components, in the CMD of Fig. 1 we cannot clearly distinguish the three RGB-MInt populations, partly because stars in the upper part of the RGB are saturated in our images, and this degrades the quality of our photometry. Therefore we cannot directly confirm the significance of all of the components proposed by Sollima et al. (2005b), despite the fact that our CMD includes a larger sample of stars because of our somewhat larger area.

The SGB offers one unique opportunity for identifying subpopulations. On the main sequence, stars that have the same composition occupy the same position regardless of age, so that different ages cannot be distinguished, while on the RGB the substructure is controlled mainly by the metallicity distribution. Thus only the SGB can be used to estimate relative ages of the various subpopulations.

Several questions naturally arise from this empirical taxonomy of the various CMD branches: 1) How does each of the 5 SGB components map into the MS and RGB components? 2) What are the age, metallicity, and helium content of each subpopulation? 3) What fraction of the total number of stars belongs to each subpopulation?

9.1. Identifying evolutionary connections between MS, SGB, and RGB

The first question can be addressed using three complementary kinds of evidence: a) the morphological continuity from one branch in the CMD to another, b) the relative numbers of stars on the various branches, and c) the spectroscopic metallicities of individual stars on the various branches. The information that is available is summarized in Table 4. Each column refers to a different section of the CMD and lists the groups that we recognize there. For each group we give the name, the percentage of the stars that belong to that group (with each column adding up to 100%), and the metallicity $[\text{Fe}/\text{H}]$. In Table 4, we indicate more than one $[\text{Fe}/\text{H}]$ value if it appears that one group

identified on the CMD may include stars belonging to different metallicity groups. MS and SGB percentages and metallicities are from the present study and P05. For the RGB we have adopted the nomenclature, percentages, and metallicities from Sollima et al. (2005b), assuming $[\text{Fe}/\text{H}] = [\text{M}/\text{H}] - 0.3$.

An inspection of the various CMDs (e.g., as in Fig. 6) allows us to identify only two quite obvious connections, namely $\text{rMS} \rightarrow \text{SGB Group A} \rightarrow \text{RGB-MP}$, and $\text{MS-a} \rightarrow \text{SGB Group D} \rightarrow \text{RGB-a}$. Further insight can come from considering the relative percentages of the groups in the different branches. Note, however, that one does not expect the relative percentages of a given population to be exactly the same in all regions of the CMD. In fact, on the MS a given magnitude interval corresponds to different stellar mass intervals for different compositions, and the evolutionary rates on the SGB and RGB are also a function of composition. However, these effects are typically at the level of 10–20% (cf. Fig. 13 in Zoccali et al. 2003) and will be ignored here.

In spite of the clear morphological connection $\text{rMS} \rightarrow \text{SGB Group A}$, this cannot be the whole story, because the percentages do not match, as is shown clearly in the first of the five sections of Table 4. The rMS makes up a much larger fraction of the MS than Group A does of the SGB; many of its stars must therefore evolve into other parts of the SGB. Since our spectroscopic investigation found that SGB Groups B and C also include stars with $[\text{Fe}/\text{H}] \sim -1.7$, we suggest that the other rMS stars evolve into these two groups, although there is no indication of the proportions. But in any case, all of the metal-poor stars with $[\text{Fe}/\text{H}] \sim -1.7$ must eventually connect to the the RGB-MP population, whose percentage is not totally inconsistent with that of the rMS group.

We now come to the helium-rich bMS population. Combining the photometric and spectroscopic information of Fig. 6 and of Figs. 17 and 18, we conclude that the bMS must continue through SGB Groups B and C, though it is not clear in what proportion.

The subsample of SGB Group B and Group C stars with $[\text{Fe}/\text{H}] \sim -1.4$ (which, given their metallicity, do not evolve into RGB-MP) must continue through RGB-MInt, as, presumably, must the stars between Groups C and D too. But

it is not clear in what proportion they occupy the different RGB-MInt branches proposed by Sollima et al. (2005b).

Finally, we note an apparent inconsistency between the percentages of SGB Group D and RGB-a; the former includes $\sim 10\%$ of the SGB stars, whereas the latter has only $\sim 5\%$ of the RGB stars, although a tight connection between the two is apparent from the morphology of the CMD. However, we also find some inconsistency between our metallicity for SGB Group D, $[\text{Fe}/\text{H}] = -1.1$, and the metallicity found by Pancino et al. (2002), $[\text{Fe}/\text{H}] = -0.6$ (an ambiguity that we also include in Table 4).

9.2. The relative ages of the subpopulations

The empirical facts that emerge from the present photometric and spectroscopic investigation can be summarized as follows:

- The stars that populate the SGB of ω Cen cover a large magnitude interval, up to ~ 1.2 in m_{F435W} or B . Four distinct SGB groups can be clearly identified, plus a possible fifth group that contributes a smaller percentage. This contrasts with what one would have expected from the MS alone, where only three distinct stellar groups can be identified.
- SGB stars in the most metal-poor group ($[\text{Fe}/\text{H}] \sim -1.7$) have a 0.3–0.4-magnitude spread in luminosity at a given color. The intermediate-metallicity group ($[\text{Fe}/\text{H}] \sim -1.4$) also shows some evidence of a similar range in SGB luminosity at a given color.
- The most metal-rich stars ($[\text{Fe}/\text{H}] \sim -1.1$) populate the faintest SGB, with a small dispersion in magnitude; however, one of them is 0.85 magnitude brighter in m_{F435W} than the others.

The most straightforward explanation for the large magnitude dispersion of the metal-poor SGB stars on the flat part of the SGB is in terms of an age difference. An age difference is also indicated by the luminosity difference among intermediate-metallicity stars that populate SGB Groups B and C, though we know that the issue is complicated by the fact that more than half of the stars in these

branches must be the progeny of the helium-rich bMS population. So for these branches we cannot firmly distinguish age effects from helium effects. It is important to note here that a spread in age has a negligible influence on the MS position, and its influence on the location of the RGB is also small. On the other hand, it has a great influence on the slope and location of the SGB in the CMD; however, the SGB location is also affected by the helium abundance.

Taking advantage of our accurate photometry and of the metallicity measurements from our spectra, we can now try to estimate the relative ages of the individual SGB stars. We do not attempt absolute age determinations here, however, because they would be sensitive to the assumed distance and reddening of the cluster, and to the photometric zero points that we have adopted. All that we assume is that the distance and the reddening are the same for all of the stars in the cluster.

For each metallicity we selected from Pietrinferni et al. (2004, 2006) a set of isochrones separated by 1 Gyr. In all cases, we assumed for the α enhancement the average of the $[\text{Ca}/\text{Fe}]$ and $[\text{Ti}/\text{Fe}]$ values from the present study. For stars having $-1.50 \leq [\text{Fe}/\text{H}] \leq -1.25$ we assumed an enhanced helium $Y = 0.38$, as was suggested in P05 for the bMS. But for high metallicity ($[\text{Fe}/\text{H}] > -1.1$, corresponding to the MS-a/SGB Group D/RGB-a population) we did not assume enhanced helium, because unlike the case of the bMS, there is no evidence for it. Note that Sollima et al. (2005a) did adopt a helium enhancement for the metal-rich population too. In any case, because of the location of the program stars on the flattest part of the SGB (cf. Figs. 17 and 18), the ages would not be strongly affected by a helium enhancement, as can be inferred from the isochrones of Pietrinferni et al. (2006); see also Fig. 6 of S05. In fact, we have verified that for $[\text{Fe}/\text{H}] > -1.4$ a change from $Y = 0.245$ to $Y = 0.35$ would move the flat part of the isochrones by an amount that corresponds to an age difference of only ~ 1 Gyr.

To estimate the age of each individual star we first shifted the isochrones in magnitude and color by adopting the same reddening and distance modulus that we used in Sect. 6 to derive the atmospheric parameters of our stars. We then calibrated the X coordinate of Fig. 4 in terms of

age, as follows. Taking advantage of the fact that in the SGB region all of the isochrones are almost parallel to the heavy line in the upper panel of Fig. 4, we derived an average X coordinate for each isochrone. We then calibrated the X coordinate as a linear function of age and metallicity, which finally allowed us to assign an age to each of our observed stars. We do not consider these reliable as absolute ages, however, so we converted them to relative ages, by assuming that the age of the oldest SGB groups corresponds to 13 Gyr (typical for a Galactic GC). The resulting relative ages are given in Table 2 for the *HST* stars, and in Table 3 for the WFI stars, and they are all plotted in Fig. 19 as a function of metallicity.

The internal errors of the relative ages shown in Fig. 19 were derived by adding in quadrature the effects of the photometric errors and the uncertainties in the metallicities. Additional errors come from the uncertainty in He content; this may affect the ages of intermediate-metallicity and metal-rich stars by ~ 1 –2 Gyr.

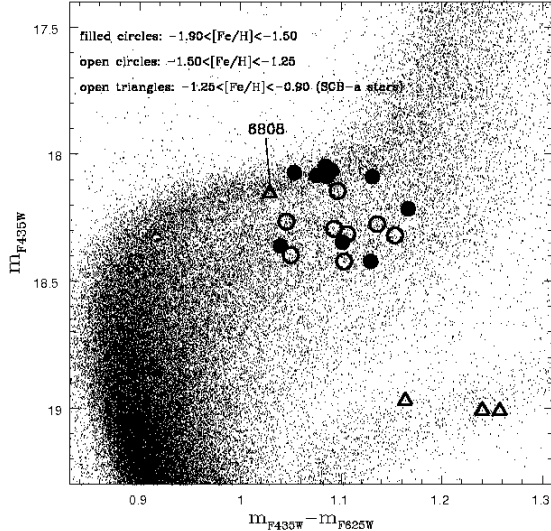


Fig. 17.— Locations of the 22 *HST* stars in the ACS CMD. Different symbols indicate different metallicity groups, as indicated in the internal label. The anomalous star 6808 is indicated. Note, here and in Fig. 18, the poor correlation between metallicity and location in the CMD.

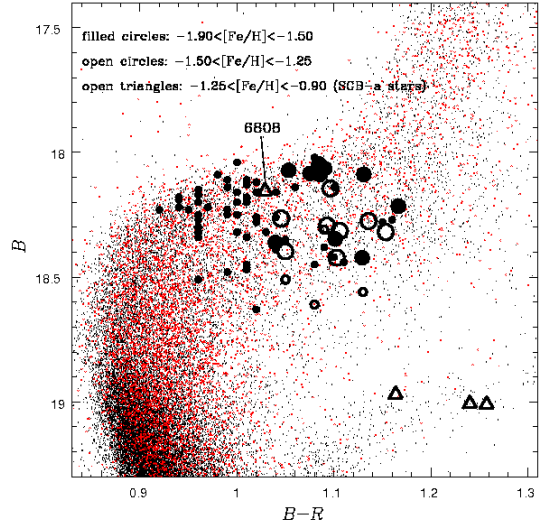


Fig. 18.— A superposition of the CMD from the *HST* photometry, transformed, according to precepts given by Sirianni et al. (2005), to ground-based B and R (small black points), and the CMD from the WFI photometry (red points). In both cases only a randomly selected subsample of all of the measured stars is plotted, in order to avoid confusion. The symbols indicate the 80 stars for which we measured the $[\text{Fe}/\text{H}]$ abundance. Different symbols indicate different metallicity groups, as indicated in the internal label. Large symbols are *HST* stars, small symbols WFI stars.

We now comment on the resulting ages as displayed in Fig. 19. Both the *HST* and the WFI samples show the same general trend. Figure 19 shows that the metal-poor stars have the largest age dispersion, and split into two distinct groups, one $\sim 30\%$ younger than the other. In absolute terms, this would correspond to an age difference of 3–4 Gyr. Within the younger and the older metal-poor groups the relative dispersion is consistent with what is expected for the error budget. Two well-defined, distinct ages for the metal-poor stars are to be favored over an age dispersion, because this is what the discrete distribution of the stars on the SGB would suggest (see Figs. 4 and 5). Our present spectroscopic sample is too small to conclude firmly whether we are dealing with two really distinct age groups, or whether there is instead a continuous distribution in ages, but

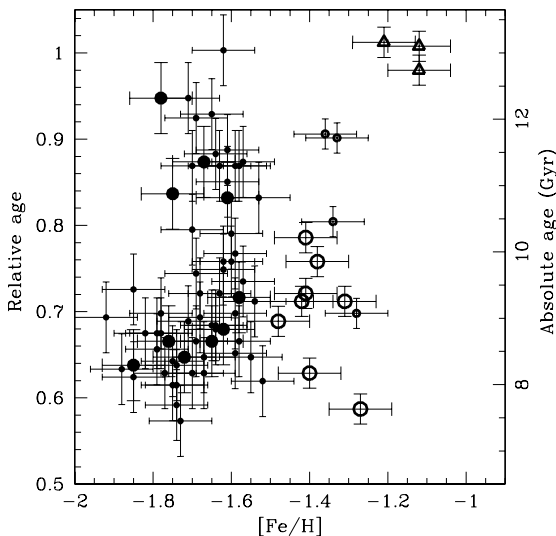


Fig. 19.— The relative ages of the target stars, plotted against their $[\text{Fe}/\text{H}]$ abundances. The left-hand axis is fractional age relative to the age of the oldest stars, which was arbitrarily assumed to be 13 Gyr. The right-hand axis is absolute age, on the same assumption. Large symbols are *HST* stars, while small ones are WFI stars. Star 6808 is omitted from this figure.

with two strong peaks at specific values. In any case, the empirical evidence is that the metal-poor SGB stars show age differences that correspond to a large fraction of the cluster age.

The intermediate-metallicity SGB stars have an age dispersion that is smaller, but still not negligible, spanning a relative age interval of about 20%, if we consider only the *HST* sample. Stars in this sample appear to be coeval with the younger of the metal-poor SGB groups. Note, however, that our intermediate-metallicity SGB stars could well include some stars with normal helium, in which case the age spread would have been overestimated.

Finally, the most metal-rich stars, SGB Group D, turn out to be as old as the oldest stars in the cluster, i.e., to be coeval with the oldest metal-poor SGB stars. Taking Fig. 19 at face value, one can hardly distinguish a unique age-metallicity relation. Rather, one can broadly distinguish four age/metallicity groups, namely, an

old metal-poor and a young metal-poor population, a young intermediate-metallicity population, and an intriguing old metal-rich population. The young components are some 30% younger than the old ones.

As a check on these relative ages estimated by isochrone fitting, we turn to another widely used method, based on the luminosity difference between the HB and the main sequence turn-off (see, e.g., Iben & Renzini 1984). We apply this method via two different approaches: First we use it to check the age of one of our SGB groups relative to that of another SGB group; then we use it to compare the age of one of the groups with that of another globular cluster.

To test the relative ages of groups, we used SGB Group A (the young metal-poor group), and SGB Group D (the old metal-rich group); these are the only groups for which the turn-off is clearly recognizable. We measured the F435W magnitudes and F435W – F625W colors of their turn-offs in our ACS photometry, and used Eq. (12) of Sirianni et al. (2005), with coefficients taken from their Table 22, to derive the V magnitudes of the two turn-offs. For the HB magnitudes we used data on RR Lyrae stars from Sollima et al. (2006a), who gave metallicities and time-averaged V magnitudes for a sample of 74 RR Lyrae stars in ω Cen. These stars make up two distinct populations, one with an average $[\text{Fe}/\text{H}] \sim -1.7$, and the other with $[\text{Fe}/\text{H}] \sim -1.2$. We identify the former as the HB progeny of the SGB-MP population and the latter as the HB progeny of our SGB Group D. In this way we were able to derive the magnitude difference between the HB and the TO for each of our two selected groups. Comparing this empirical difference with the theoretical one derived from the models by Pietrinferni et al. (2004, 2006), we indeed confirm that SGB Group A appears to be $\sim 30\%$ younger than the SGB Group D population.

We also followed an alternative approach, comparing SGB Group A directly with another GC of similar metallicity, M13. From Sollima et al. (2006a) we know that the average luminosity of the metal-poor RR Lyraes in ω Cen is $\langle V \rangle = 14.4$, and we estimate $V = 14.6 \pm 0.1$ for the lower envelope of the RR Lyrae distribution, which corresponds to the zero-age HB. In order to avoid transforming from the ACS photometric bands of Fig. 1

to the Johnson V band, we used our WFI photometry, and estimated $V_{\text{MSTO}} = 18.10 \pm 0.25$ for SGB Group A. Thus we have $\Delta V_{\text{MSTO}}^{\text{HB}} = 3.5 \pm 0.3$. This value, though very uncertain, is typical for old globular clusters with intermediate metallicities. De Angeli et al. (2005) find a nearly identical value of $\Delta V_{\text{MSTO}}^{\text{HB}}$ for M13, a cluster whose metal content is similar to that of SGB Group A. However, we have argued that SGB Group A represents the youngest component in ω Cen; hence the older components would be significantly older than typical globular clusters, possibly resulting in an age that is embarrassingly old compared with that of the universe. We note at the same time that S05 needed an age of 16 Gyr to fit ω Cen (although we are reluctant to consider absolute ages in any case). Moreover, De Angeli et al. find for the GC M3, whose metallicity is also similar, an age only 3/4 as great as that of M13—perhaps not so surprising, however, since M3 and M13 are a well-known “second-parameter pair”. This intriguing aspect requires further study, including a more accurate estimate of $\Delta V_{\text{MSTO}}^{\text{HB}}$ and, most importantly, a more thorough spectroscopic exploration of the various SGBs and HB components. Available spectroscopic data are still not sufficient to explore the absolute ages of the various components of ω Cen.

Large age differences among the stars of ω Cen are not a new finding. Smith et al. (2000), by analyzing the pattern of s-process elements, suggested a prolonged process of star formation, lasting of the order of 2–3 Gyr. Hilker & Richtler (2000, 2002) argued for an extended star-formation period of up to 6 Gyr. Rough estimates of ages, both from broad- and narrow-band photometry, also show a large age spread, as presented by Hilker and Richtler (2000), Rey et al. (2004), and Hughes et al. (2004). An age-metallicity relation was found by Stanford et al. (2003) from a combined photometric and spectroscopic study, with a mean age difference of 4–5 Gyr between the stars at $[\text{Fe}/\text{H}] = -1.7$ (our oldest SGB metal-poor group) and those at $[\text{Fe}/\text{H}] \simeq -1.4$ (our youngest intermediate-metallicity group). Hilker et al. (2004) also find an age dispersion, and they find an age-metallicity relation for stars with $[\text{Fe}/\text{H}] < -1.0$, with a difference of about 6 Gyr between the youngest and oldest stars in their sample; however, the young component of the

metal-poor group is absent from their picture.

By contrast S05, using the same *HST* images that we used here and metallicities derived from the Ca II triplet, concluded that all groups are substantially coeval, within the ± 2 -Gyr uncertainty that affects their estimates. Our results agree with theirs only in that the most metal-rich component (SGB Group D = SGB-a) is found to be coeval with the oldest metal-poor group. Conversely, the strongest evidence for age differences comes from the luminosity differences among metal-poor SGB stars that we have documented here for the first time. We also note that S05 can argue for coeval subpopulations only after assuming a different helium content for each of them, rather than only for the bMS component, as in the present study.

In closing this section, we emphasize that we refer to age differences, as opposed to simply an age spread. This is justified by the clearly discrete structure of the SGB, which argues in favor of distinct episodes of star formation rather than a continuous, albeit fluctuating, star-formation history. We believe that this discreteness, together with a broken age-metallicity relation (with some metal-poor stars being younger than some metal-rich ones), puts strong constraints on possible formation scenarios for this puzzling stellar system.

10. Discussion

Based on deep *HST* photometry of the central regions of ω Cen, and on high-resolution spectroscopy of a sample of SGB stars in the cluster, we have identified and characterized four distinct age/metallicity groups of stars. These groups include over 90% of the cluster population in the region that we have explored; our data do not allow us properly to characterize the remaining part.

These groups include:

1. An old and metal-poor population ($[\text{Fe}/\text{H}] \sim -1.7$), with an age that we assume to be that of the oldest GCs of the Milky Way, ~ 13 Gyr. This group appears to populate primarily the SGB Group C component, and makes up about a third of the metal-poor population of the cluster. Note, however, that because of photometric errors it is sometime difficult to tell whether an individual star belongs to SGB Group B or to

Group C.

2. A young metal-poor group ($[\text{Fe}/\text{H}] \sim -1.7$), on average up to 3–4 Gyr younger than the previous group. This group (our SGB Group A) includes about 33% of the ω Cen SGB stars, and makes up the remaining two thirds of the metal-poor SGB population.
3. A young intermediate-metallicity group, with $[\text{Fe}/\text{H}] \sim -1.4$. It appears to be nearly coeval with the young metal-poor component. This group seems to populate primarily (but not exclusively) SGB Group B, and, because of its metallicity, may be connected to the bMS component. If so, it should be helium rich, and include about a third of the SGB stars in this central region of the cluster where our observations are.
4. An old metal-rich group for which we find $[\text{Fe}/\text{H}] \sim -1.1$, although both its average metallicity and the extent of a possible metallicity dispersion remain to be established better. For the metallicity that we have adopted, this group appears to be as old as the old metal-poor group, i.e., with an age of the order of our assumed age for the oldest population (~ 13 Gyr). Its age would decrease by ~ 1.5 Gyr if we were to adopt the higher metallicity $[\text{Fe}/\text{H}] = -0.6$ that is favored by Sollima et al. (2005a). The group is confined to the region of SGB Group D, and includes $\sim 10\%$ of the SGB stars in the part of ω Cen that we have explored. On the RGB side it connects to the RGB-a sequence of Pancino et al. (2000), and on the main-sequence side it connects to the MS-a component that we have identified in Sect. 3 (see Fig. 3).
5. In addition, we have identified a group of stars, including about 8% of the cluster SGB population, that spread between SGB Groups C and D. No metallicity information is available for this small component, so that we cannot say anything about its age.

The first four groups can readily be recognized in Fig. 19, and the occasional ambiguity in assigning stars to either SGB Group B or Group C can be appreciated in Figs. 17 and 18.

10.1. Formation and evolution of the cluster

The diversity of ages and metallicities displayed in Fig. 19 eliminates once and for all the possibility that ω Centauri had its origin in a single progression of star formation and metal enrichment. There is no way in which, within the gravitational domain of a globular cluster, gas masses with different chemical compositions could have maintained separate identities until the time of latest star formation.

The structure of Fig. 19 bespeaks a multiplicity of origins. Indeed, a single developing population would follow a line that from the top left slopes downward and to the right, tracing the increase of metallicity with time. In Fig. 19 only the old metal-poor stars, joined with the younger intermediate-metallicity stars, could satisfy this chemical-enrichment criterion, even within the uncertainties of our ages and metallicities. However, the most metal-rich population, with its extreme old age, cannot fit into such a scheme. Rather, it must have come from a brief star-forming episode in a different region, where enrichment had proceeded very rapidly. By contrast, the large clump of points at the lower left, which seems to slope in the wrong sense, defies any simple chemical-evolution scenario. Overall, the mix of ages and metallicities in ω Centauri suggests multiple birth locations, followed by a later merging process.

This need for late merging seems to exclude the possibility of explaining ω Centauri as a merger of several of the fragments that went to make up the early Milky Way. Our Galaxy must have been fully formed, at least in its initial incarnation, long before the youngest metal-poor stars of ω Cen were born. Since the merger of several Milky Way globular clusters seems very unlikely, because of their small target cross-sections, we are led to the often-made suggestion that the cluster that we now see is the remnant of a dwarf galaxy that was captured by the Milky Way; what remains of it today would be the central core that was bound tightly enough to resist the tidal buffeting that removed the outer parts of the system. Such a central core could easily contain a broad mixture of the populations that had made up that galaxy. In order to allow time for the separate development of all the populations that we see, the cap-

ture must have taken place several billion years after the birth of the Milky Way. The capture must have taken place far enough in the past, however, for tidal forces and orbital spreading to have dissipated any residual stream, such as the one in which the Sagittarius dwarf is still embedded. We also note that all four main age/metallicity components appear to be enhanced in α elements (see Fig. 16). Following the canonical interpretation, this would imply that each component underwent rapid chemical enrichment (hence remained dominated by SNI nucleosynthetic products), in spite of the large age differences among them.

The above conclusions seem fairly well established, but an alternative explanation has been advanced, which should be dismissed once and for all. It has been suggested, e.g. by Ferraro et al. (2004) and by Freyhammer et al. (2005), that the stars that define some of the sequences discussed above might lie at a distance different from that of the other stars of the cluster. It strains credulity, however, to suggest that the mixture of populations could be explained by a simple alignment effect, since this would require two or more rich clusters along the same direction in the sky, with very similar radial velocities (as pointed out by P05, and shown in more detail in Sect. 4 of the present paper) and proper motions (whose similarity was shown by Anderson 2003). An alternative might be to assume that ω Cen is a very elongated object, and that we are looking at it along its major axis, but such an implausible structure would not be able to survive the strong dynamical interactions that ω Cen has with the Galaxy. Finally, the CMD in Fig. 1 shows that the most metal-rich population has a MS that is clearly on the red side of the other populations, in sharp disagreement with an explanation of this sequence as a difference in distance.

Further insight into the formation history of ω Cen may come from the internal distribution of the various subpopulations. Stars with different metal content appear to have a different radial distribution (Norris et al. 1996), qualitatively consistent with the radial gradient in the bMS/rMS ratio reported by Sollima et al. (2006b). Moreover, an asymmetric distribution with respect to the cluster center has been suggested by Jurcsik (1998) and by Pancino et al. (2003). As a separate complication, Calamida et al. (2005) have

claimed that ω Cen is affected by differential reddening. However, the sharpness of the sequences in our Figures 1–6, especially SGB Group D and the upper edge of the MS turn-off region, suggests that the existence of any serious differential reddening is very unlikely.

Two more issues related to chemical abundances need to be addressed: the $[\alpha/\text{Fe}]$ ratios of the various subpopulations, and the origin of the helium enhancement that seems to exist in at least one of them. All 22 stars for which we have measured abundances of individual elements are high in Ca and Ti, indicating $[\alpha/\text{Fe}] \sim 0.3\text{--}0.4$, irrespective of their membership in the various subpopulations (Pancino et al. (2002) found $[\alpha/\text{Fe}] \sim 0.10$ for RGB-a; as we mentioned previously for $[\text{Fe}/\text{H}]$, there is a discrepancy between their results and ours. We note however, that their abundance study, like ours, included only three stars that belong to this population.)

An alpha enhancement is generally interpreted as evidence for prompt chemical enrichment, over a time scale shorter than the typical delay with which Type Ia supernovae released the bulk of the iron. This delay is traditionally assumed to be of the order of 1 Gyr, i.e., significantly shorter than the age differences that we have estimated for the various subpopulations. The fact that all components appear to be enhanced in α elements again argues for a short duration of the enrichment processes that preceded the formation of all the cluster subpopulations.

Following Norris (2004) and Bedin et al. (2004), we share the view that the bMS component is enriched in helium. This is one of the most puzzling aspects of this exceptional object. When did the helium enrichment take place—before or after this population merged with the rest of the body of ω Cen? Are other subpopulations enriched in helium? The available data do not allow us to venture an answer to these questions. However, our understanding of the formation history of this object will not be complete as long as they remain unanswered.

Finally, we should not forget star 6808 (the brightest open triangle in Figs. 17 and 18). As discussed in previous sections, we consider its metallicity and its position in the CMD to be quite well established. Still, it is a quite unusual star, in that it has the metallicity of SGB Group D but is

0.85 magnitude brighter in the m_{F435W} band than any other star in this group. It is very unlikely to be a field-star contaminant, because it lies in the central part of the cluster and its radial velocity and proper motion agree well with those of the cluster. Star 6808 could be evidence of an extreme anomaly, an age difference of 5 or more Gyr within the metal-rich population. Alternatively, in a less extreme interpretation we might suggest that star 6808 is possibly a blue straggler, related to the SGB Group D population, even though it seems *a priori* very unlikely for us to have encountered one such star among only four stars that turned out to be metal rich. A more extended spectroscopic campaign could help to clarify this last issue too.

The authors wish to thank the referee, John Norris, for his careful reading of the manuscript, and for stimulating comments. This project has been partially supported by the Italian MIUR, under the program PRIN2003. J. A. and A. M. C. acknowledge support by STScI grant GO-9442, I. R. K. support by grant GO-10101.

REFERENCES

- Alonso, A., Arribas, S., & Martinez-Roger, C. 1996, *A&A*, 313, 873
- Alonso, A., Arribas, S., & Martnez-Roger, C. 1999, *A&A*, 140, 261
- Anderson, J. 1997, Ph.D. thesis, Univ. California, Berkeley
- Anderson, J. 2003, *ASPCS*, 296, 125
- Anderson, J., Bedin, L. R., Piotto, G., Yadav, R. S., & Bellini, A. 2006, *A&A*, 454, 1029
- Anderson, J., & King, I. R. 2006, ACS Instrument Science Report 2006-01 (Baltimore: STScI)
- Bedin, L. R., Piotto, G., Anderson, J., Cassisi, S., King, I. R., Momany, Y., & Carraro, G. 2004, *ApJ*, 605, 125 (B04)
- Bedin, L. R., Cassisi, S., Castelli, F., Piotto, G., Anderson, J., Salaris, M., Momany, Y., & Pietrinferni, A., 2005, *MNRAS*, 357, 1038
- Blecha, A., Cayatte, V., North, P., Royer, F., & Simond, G. 2000, *Proc. SPIE*, 4008, 467
- Brown, J.A. & Wallerstein, G. 1993, *AJ*, 106, 133
- Calamida, A., Stetson, P. B., Bono, G., Freyhammer, L. M., Grundahl, F., Hilker, M., Andersen, M. I., Buonanno, R., Cassisi, S., Corsi, C. E., Dall’Ora, M., Del Principe, M., Ferraro, I., Monelli, M., Munteanu, A., Nonino, M., Piersimoni, A. M., Pietrinferni, A., Pulone, L., & Richtler, T. 2005, *ApJ*, 634, L69
- Caldwell, J. A. R., Cousins, A. W. J., Ahlers, C. C., van Wamelen, P., & Maritz, E. J. 1993, *SAAO Circulars*, 15
- De Angeli, F., Piotto, G., Cassisi, S., Busso, G., Recio-Blanco, A., Salaris, M., Aparicio, A., & Rosenberg, A. 2005, *AJ*, 130, 116
- Ferraro, F. R., Sollima, A., Pancino, E., Bellazzini, M., Straniero, O., Origlia, L., & Cool, A. M. 2004, *ApJ*, 603, 81
- Freyhammer, L. M., Monelli, M., Bono, G., Cunti, P., Ferraro, I., Calamida, A., Degl’Innocenti, S., Prada Moroni, P. G., & Del Principe, M., Piersimoni, A. 2005, *AJ*, 623, 860
- Gratton, R. G., Sneden, C., Carretta, E., Bragaglia, A. 2000, *A&A*, 354, 169
- Hilker, M., & Richtler, T. 2000, *A&A*, 362, 895
- Hilker, M., & Richtler, T. 2002, *ASPCS*, 265, 59
- Hilker, M., Kayser, A., Richtler, T., & Willemsen, P. 2004, *A&A*, 422, 9
- Houdashelt, M. L., Bell, R. A., & Sweigart, A. V. 2000, *AJ*, 119, 1448
- Hughes, J., Wallerstein, G., van Leeuwen, F., Hilker, M. 2004, *AJ*, 127, 980
- Iben, I. Jr., & Renzini, A. 1984, *Phys. Rep.* 105, 329
- Izzard, R. G., Tout, C. A., Karakas, A., & Pols, O. R. 2004, *MNRAS*, 350, 407
- Jurcsik, J. 1998, *ApJ*, 506, 113
- Kurucz, R. L. 1992, in *IAU Symp. 149, The Stellar Populations of Galaxies*, ed. B. Barbuy & A. Renzini (Dordrecht: Reidel), 225

- Lee, Y. W., Joo, S. J., Han, S. I., Chung, C., Ree, C. H., Sohn, Y. J., Kim, Y. C., Yoon, S. J., Yi, S. K., & Demarque, P. 2005, *ApJ*, 621, 57
- Maeder, A., & Meynet, G. 2006, *A&A*, 448, 37
- Meylan, G. 2003, *ASPCS*, 296, 17
- Norris, J. E., & Da Costa, G. S. 1995, *ApJ*, 447, 680
- Norris, J. E. Freeman, K. C., & Mighell, K. J. 1996, *ApJ*, 462, 241
- Norris, J. E. 2004, *ApJ*, 612, 25
- Pancino, E., Ferraro, F. R., Bellazzini, M., Piotto, G., & Zoccali, M. 2000, *ApJ*, 534, 83
- Pancino, E., Pasquini, L., Hill, V., Ferraro, F. R., & Bellazzini, M. 2002, *ApJ*, 568, 101
- Pancino, E., Seleznev, A., Ferraro, F. R., Bellazzini, M., & Piotto, G. 2003, *MNRAS*, 345, 683
- Pietrinferni, A., Cassisi, S., Salaris, M., & Castelli, F. 2004, *ApJ*, 612, 168
- Pietrinferni, A., Cassisi, S., Salaris, M., & Castelli, F. 2006, *ApJ*, 642, 797
- Piotto, G., Villanova, S., Bedin, L. R., Gratton, R., Cassisi, S., Momany, Y., Recio-Blanco, A., Lucatello, S., Anderson, J., King, I. R., Pietrinferni, A., & Carraro, G. 2005, *ApJ*, 621, 777 (P05)
- Reijns, R. A., Seitzer, P., Arnold, R., Freeman, K. C., Ingerson, T., van den Bosch, R. C. E., van de Ven, G., & de Zeeuw, P. T. 2006, *A&A*, 445, 503
- Rey, S. C., Lee, Y. W., Ree, C. H., Joo, J. M., Sohn, Y. J., & Walker, A. R. 2004, *AJ*, 127, 958
- Salaris, Maurizio, Chieffi, Alessandro, & Straniero, Oscar 1993, *ApJ*, 414, 580
- Sekiguchi, M., & Fukugita, M. 2000, *AJ*, 120, 1072
- Sirianni, M., Jee, M. J., Bentez, N., Blakeslee, J. P., Martel, A. R., Meurer, G., Clampin, M., De Marchi, G., Ford, H. C., Gilliland, R., Hartig, G. F., Illingworth, G. D., Mack, J., & McCann, W. J. 2005, *PASP*, 117, 1049
- Smith, V. V., Suntzeff, N. B., Cunha, K., Gallino, R., Busso, M., Lambert, D. L., & Straniero, O. 2000, *AJ*, 119, 1239
- Sollima, A., Pancino, E., Ferraro, F. R., Bellazzini, M., Straniero, O., Pasquini, & L. 2005a, *ApJ*, 634, 332 (S05)
- Sollima, A., Ferraro, F. R., Pancino, E., & Bellazzini, M. 2005b, *MNRAS*, 357, 265
- Sollima, A., Bossirova, J., Catelan, M., Smith, H.A., Minniti, D., Cacciari, C., & Ferraro, F.R. 2006a, *ApJ*, 640, 43
- Sollima, A., Ferraro, F.R., Bellazzini, M., Origlia, L., Straniero, O., & Pancino E. 2006b, *astro-ph/0609650*
- Stanford, L. M., Cannon, R. D., Da Costa, G. S., Norris, J. E., & Croke, B. F. 2003, *IAU JD*, 4, 15
- Stanford, L. M., Da Costa, G. S., Norris, J. E., Cannon, R. D. 2006, *ApJ*, 647, 1075
- Straizys, V., & Kuriliene, G. 1981, *Ap&SS*, 80, 353
- Suntzeff, N. B., & Kraft, R. P. 1996, *AJ*, 111, 191
- Tornambè, A., & Matteucci, F. 1986, *MNRAS* 223, 69
- van de Ven, G., van den Bosch, R. C. E., Verolme, E. K., & de Zeeuw, P. T. 2006, *A&A*, 445, 513
- Zoccali, M., Renzini, A., Ortolani, S., Greggio, L., Saviane, I., Cassisi, S., Rejkuba, M., Barbuy, B., Rich, R. M., & Bica, E. 2003, *A&A*, 399, 931

This 2-column preprint was prepared with the AAS L^AT_EX macros v5.2.

TABLE 3
OBSERVED SGB-WFI STARS.

ID	R.A.(J2000.0)	Decl.(J2000.0)	V	$B - V$	$V - I_C$	$V - R_C$	RV_H (km/s)	T_{eff} (K)	$\log g$	[Fe/H]	Age
SGB-MP + SGB-MInt2 stars											
12310	201.580363	-47.653532	17.54	0.57	0.84	0.42	218	5795	3.9	-1.75	0.61
12496	201.664258	-47.652604	17.46	0.58	0.79	0.42	219	5807	3.9	-1.73	0.57
14612	201.554592	-47.641987	17.53	0.56	0.79	0.42	228	5843	4.0	-1.74	0.59
14716	201.633617	-47.641492	17.54	0.57	0.82	0.44	232	5775	3.9	-1.67	0.63
15257	201.598488	-47.638770	17.62	0.55	0.77	0.41	217	5909	4.0	-1.77	0.63
15328	201.506173	-47.638341	17.57	0.57	0.79	0.39	222	5896	4.0	-1.74	0.61
16128	201.549683	-47.634763	17.63	0.55	0.79	0.39	245	5942	4.0	-1.52	0.62
16212	201.572946	-47.634394	17.39	0.62	0.87	0.46	221	5594	3.8	-1.85	0.62
16385	201.648017	-47.633606	17.70	0.55	0.75	0.41	215	5943	4.1	-1.65	0.68
17389	201.491942	-47.629072	17.53	0.59	0.83	0.43	240	5759	3.9	-1.67	0.65
17559	201.632454	-47.628463	17.64	0.56	0.78	0.40	229	5913	4.0	-1.59	0.65
19322	201.579104	-47.621130	17.73	0.55	0.77	0.41	208	5906	4.1	-1.78	0.70
19930	201.480925	-47.618674	17.57	0.57	0.81	0.42	208	5805	3.9	-1.88	0.63
20004	201.513454	-47.618406	17.66	0.56	0.81	0.42	221	5839	4.0	-1.59	0.70
20055	201.667229	-47.618346	17.67	0.55	0.77	0.42	216	5892	4.0	-1.78	0.67
21948	201.595187	-47.610929	17.58	0.58	0.83	0.44	215	5748	3.9	-1.82	0.67
23057	201.662250	-47.606833	17.62	0.58	0.80	0.42	242	5826	4.0	-1.64	0.68
24029	201.661362	-47.603400	17.50	0.63	0.88	0.47	218	5559	3.8	-1.85	0.73
24141	201.428288	-47.602701	17.64	0.55	0.77	0.39	207	5953	4.0	-1.70	0.63
24410	201.467408	-47.601893	17.58	0.58	0.82	0.42	241	5780	3.9	-1.79	0.66
24503	201.449554	-47.601526	17.70	0.54	0.78	0.39	220	5961	4.1	-1.74	0.64
25948	201.539033	-47.596667	17.46	0.63	0.89	0.46	245	5575	3.8	-1.79	0.67
6791	201.658221	-47.687012	17.67	0.56	0.75	0.39	228	5972	4.1	-1.58	0.67
9018	201.664329	-47.672232	17.67	0.55	0.75	0.39	238	5993	4.1	-1.55	0.65
10012	201.542692	-47.665885	17.68	0.59	0.82	0.42	235	5772	4.0	-1.62	0.76
10328	201.695171	-47.664269	17.91	0.56	0.81	0.45	247	5787	4.1	-1.64	0.88
11471	201.638833	-47.658108	17.67	0.58	0.80	0.41	223	5842	4.0	-1.54	0.71
12553	201.602463	-47.652263	17.67	0.58	0.81	0.42	224	5811	4.0	-1.63	0.72
15472	201.615946	-47.637784	17.77	0.55	0.76	0.41	217	5934	4.1	-1.57	0.73

TABLE 3—Continued

ID	R.A.(J2000.0)	Decl.(J2000.0)	V	$B - V$	$V - I_C$	$V - R_C$	RV_H (km/s)	T_{eff} (K)	$\log g$	[Fe/H]	Age
15544	201.709317	-47.637547	17.67	0.56	0.77	0.39	241	5943	4.0	-1.69	0.67
15948	201.591800	-47.635583	17.78	0.56	0.76	0.40	226	5936	4.1	-1.62	0.75
17310	201.606596	-47.629565	17.67	0.60	0.79	0.43	221	5780	4.0	-1.69	0.74
19573	201.722675	-47.620179	17.54	0.60	0.83	0.41	241	5760	3.9	-1.75	0.64
23277	201.765721	-47.606009	17.68	0.58	0.87	0.46	247	5681	4.0	-1.60	0.76
25395	201.653267	-47.598729	17.61	0.59	0.81	0.42	218	5785	4.0	-1.68	0.69
27030	201.709167	-47.593225	17.74	0.58	0.82	0.42	240	5795	4.0	-1.59	0.77
27176	201.731092	-47.592774	17.56	0.59	0.86	0.44	216	5694	3.9	-1.71	0.69
6308	201.663075	-47.690455	17.73	0.57	0.73	0.39	220	5967	4.1	-1.68	0.72
7037	201.578883	-47.685244	17.58	0.60	0.79	0.41	228	5812	4.0	-1.64	0.68
10822	201.571267	-47.661535	17.94	0.57	0.76	0.39	232	5927	4.1	-1.70	0.87
12382	201.719504	-47.653239	18.03	0.60	0.80	0.42	239	5788	4.1	-1.62	1.00
13612	201.661137	-47.646816	17.92	0.65	0.86	0.49	244	5569	4.0	-1.36	0.85
13906	201.720854	-47.645374	17.71	0.62	0.82	0.42	231	5740	4.0	-1.70	0.80
17912	201.651671	-47.627033	17.62	0.65	0.90	0.50	228	5504	3.9	-1.63	0.87
18508	201.648763	-47.624502	17.89	0.62	0.81	0.42	229	5770	4.1	-1.34	0.77
19626	201.576500	-47.619906	17.80	0.60	0.83	0.45	238	5714	4.0	-1.61	0.85
19778	201.626646	-47.619421	17.75	0.63	0.85	0.46	242	5620	4.0	-1.61	0.89
20268	201.638696	-47.617553	17.59	0.68	0.90	0.48	220	5463	3.8	-1.59	0.87
23171	201.728758	-47.606451	17.53	0.61	0.89	0.45	240	5619	3.9	-1.92	0.69
24735	201.579258	-47.600892	17.83	0.63	0.83	0.46	230	5641	4.0	-1.65	0.93
25115	201.674296	-47.599680	17.83	0.60	0.88	0.50	242	5567	4.0	-1.71	0.95
25250	201.487533	-47.598979	17.77	0.65	0.87	0.45	231	5572	4.0	-1.69	0.92
28869	201.584737	-47.587474	17.85	0.60	0.80	0.41	235	5808	4.1	-1.58	0.87
6493	201.671692	-47.689141	17.89	0.58	0.77	0.41	230	5873	4.1	-1.57	0.87
8307	201.662962	-47.676813	17.73	0.61	0.80	0.40	242	5820	4.0	-1.60	0.79
8675	201.539787	-47.674428	17.95	0.66	0.82	0.42	235	5694	4.1	-1.33	0.85
9271	201.597104	-47.670620	17.74	0.61	0.83	0.44	225	5719	4.0	-1.53	0.83
9352	201.569362	-47.670094	17.66	0.65	0.82	0.44	222	5694	4.0	-1.28	0.68

TABLE 4

IDENTIFIED STELLAR POPULATIONS

MS	SGB	RGB
rMS	SGB Group A	RGB-MP
57%	33%	42±8%
-1.7	-1.7	-1.7
bMS	SGB Group B	RGB-MInt1
33%	29%	28±6%
-1.4	-1.7 and -1.4	-1.5
	SGB Group C	RGB-MInt2
	20%	17±5%
	-1.7 and -1.4	-1.2
	?	RGB-MInt3
	8%	8±3%
	-1.1?	-1.0
MS-a	SGB Group D	RGB-a
10%(?)	10%	5±1%
-1.1 and/or -0.6	-1.1 and/or -0.6	-0.8